Optical quantification of molecular interaction strength in protein condensates

Timon Beck[1, 2, 3], Lize-Mari van der Linden[3 †], Wade M. Borcherds [4 †], Kyoohyun Kim[1, 2], Raimund Schlüßler[3], Paul Müller[1, 2], Titus Franzmann[3], Conrad Möckel[1, 2], Ruchi Goswami[1, 2], Mark Leaver[5], Tanja Mittag[4], Simon Alberti[3], and Jochen Guck[1, 2, 6, *]

[1]Max Planck Institute for the Science of Light, Erlangen, Germany
[2]Max-Planck-Zentrum für Physik und Medizin, Erlangen, Germany
[3]Biotec, TU Dresden, Dresden, Germany
[4]Department of Structural Biology, St. Jude Children's Research Hospital, Memphis, TN, USA
[5]Max Planck Institute of Molecular Cell Biology and Genetics, Dresden, Germany
[6]Department of Physics, Friedrich-Alexander Universität Erlangen-Nürnberg (FAU), Erlangen, Germany
[†]equal contribution
[*]jochen.guck@mpl.mpg.de

March 19, 2024

Abstract

Biomolecular condensates have recently been identified as a ubiquitous means of intracellular organization. Investigating the molecular interactions determining the formation, and physical properties of biomolecular condensates provides key insights for understanding their biological function, and dysfunction. Here, we applied Brillouin microscopy and quantitative phase imaging to quantify average molecular interaction strength, dry mass density, and protein volume fraction in protein condensates in vitro. We monitored the physical changes in FUS condensates in response to altering temperature and ion concentration. Conditions favoring phase separation increased Brillouin shift, linewidth, and dry mass density. In contrast to solidification by chemical crosslinking, physical aging of condensates had only a small impact on the Brillouin shift. Physical aging was suppressed at a high ion concentration. Finally, we characterized sequence variations of the low-complexity domain of hnRNPA1 that change the driving force for phase separation and found that they also alter the physical properties of the condensates. Our results provide a new experimental perspective on the physical properties of protein condensates and their sensitivity to solution conditions, sequence, and as a function of time.

1 Introduction

Cells organize their complex inner structure to control the reactions of different components in space and time. This can be achieved by enclosing specific parts of the cellular interior within a membrane, as is the case for the nucleus, mitochondria, or transport vesicles. Another way, which has attracted increasing interest in recent years, is the formation of membraneless compartments via phase separation. Phase separation of macromolecules into a condensed phase occurs above threshold concentrations of the macromolecules, and the driving force for phase separation is modulated by the concentration of ions, molecular crowders, and ligands, and by physical parameters such as temperature [1, 2]. Such condensates are viscoelastic fluids, but they can also transition into viscoelastic solids [3] or solid cross-beta fibrils [4, 5] — a state often associated with pathology. For example, mutations in the fused in sarcoma (FUS) and hnRNPA1 proteins investigated in this study are implicated in a spectrum of neurodegenerative diseases, including amyotrophic lateral sclerosis (ALS) [6, 7].

For the characterization of the complex viscoelastic properties that biological condensates may exhibit, or to uncover the underlying molecular interactions, the state of the art comprises the use of a set of techniques reporting on different characteristics. A molecular perspective, that is for example taken by nuclear magnetic resonance (NMR) [8] or Förster resonance energy transfer (FRET) [9], helps to understand single residue dynamics and specific interaction patterns. For a more general characterization of bulk material properties, however, different approaches are needed. A common method used in the field is fluorescence recovery after photobleaching (FRAP). Assuming a purely viscous fluid, FRAP can be used for a qualitative assessment of relative viscosity [10]. Challenges of this technique mainly arise due to the required assumptions about the system probed and the consequential difficulty obtaining robust quantitative values [11]. Condensate coalescence times are typically utilized to determine inverse capillary velocities, which can be converted to surface tensions with the knowledge of viscosities – again assuming a purely viscous fluid [12]. Optical traps [10, 13, 14] or tracking of tracer particles [15] allow the extraction of complex elastic moduli, providing direct insight into the viscoelastic properties of condensates. The incorporation of beads or tracer particles into the condensates, however, can be experimentally cumbersome and potentially influence the results obtained.

Moreover, a simple measure of molecular interaction strengths applicable to all states of matter found in biological condensates is not yet available. With these challenges in mind, we chose a purely optical, label-free approach, that

does not require extensive assumptions and reports on macroscopic material properties and average molecular interaction strength. We employed Brillouin microscopy to investigate biological phase separation at intermediate length and timescales by quantifying the average molecular interaction strength that drives collective molecular motion. One form of collective molecular motion is a thermally excited pressure wave (Figure 1) propagating through a material at the speed of sound, v. Light that is scattered by such a propagating wave experiences a frequency shift ν_{B}, called Brillouin shift. This type of inelastic light scattering was described theoretically by Brillouin and Mandelstam [16, 17] in the 1920s. The absolute value of the Brillouin shift is proportional to the speed of sound, which is determined by longitudinal modulus M and mass density ρ as $v = \sqrt{M/\rho}$. The longitudinal modulus can be interpreted as an average molecular coupling constant, giving rise to a resistance against uniaxial compression. Important to note is that this resistance is not specific to a particular type of molecule (e.g., proteins); any molecule within the probed volume contributes. A stronger coupling between molecules gives rise to a higher sound velocity and a greater Brillouin shift ($M \propto \nu_{\mathrm{B}}^2$). The molecular motion probed takes place in the sub-nanosecond regime and averages molecular interactions over a few hundred nanometers.
While the Brillouin shift is associated with the elastic properties of the material (i.e., the longitudinal modulus), the linewidth Δ_{B} is related to dissipation. In a liquid that is homogeneous on the length scale of the sound wave, sound attenuation is determined by the internal degrees of freedom of the material that dissipate energy and give rise to its viscosity [18, 19].

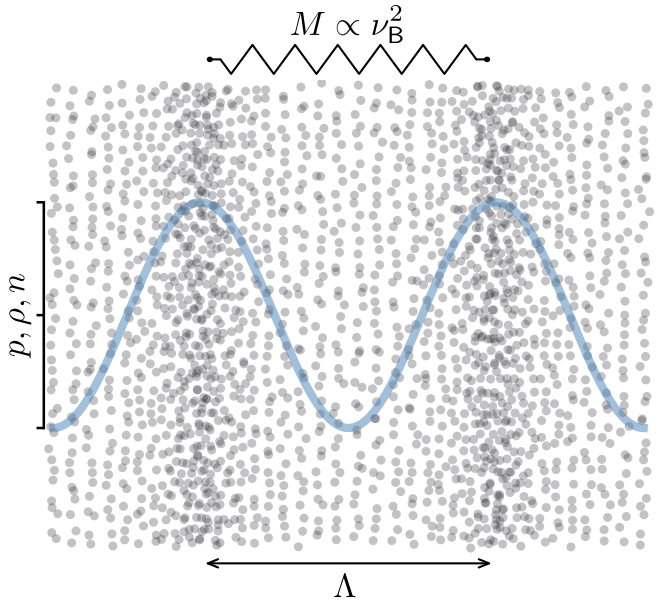

Figure 1: Illustration of a thermally excited pressure wave. Individual particles are indicated as grey dots, the blue line indicates the change in pressure, density, and refractive index compared to an unperturbed state. The amplitude of the wave and the corresponding particle displacement are exaggerated for better visualization. Due to the pressure wave, particles get pushed together (high pressure) or pulled apart (low pressure). (Inter)molecular interactions give rise to an inherent resistance to this collective particle displacement. This resistance can be quantified by the longitudinal modulus M, an average molecular coupling constant on the length scale of the acoustic wavelength Λ, which is in our case on the order of a few hundred nm corresponding to an acoustic frequency in the GHz regime. Stronger particle interactions lead to a higher longitudinal modulus and faster pressure wave propagation. As the pressure p is coupled to density ρ and consequently refractive index n, periodic changes in pressure can scatter light (Brillouin scattering).

While the application of Brillouin microscopy for biophysical research is a relatively recent development [18, 20], the investigation of viscoelasticity with sound waves has a long history. Ultrasonic investigations were used broadly in material science and polymer physics, as well as to study phase separation [21, 22]. One specific advantage of using a sound-based method to study protein condensates is the possibility to quantitatively characterize material properties in any state of matter. There is no limitation to liquids or solids; in the case of Brillouin microscopy, optical accessibility is the only requirement. Furthermore, the determination of mechanical properties does not involve the application of a mechanical model which requires certain assumptions about the system probed. This is particularly advantageous for samples where the state of matter is not known or changes over time. Brillouin microscopy has already been applied to membraneless organelles. While other groups have previously studied nucleoli [23] and FUS-condensates in fixed cells [24]], our group has recently, employed a combination of spatially resolved refractive index measurements and Brillouin microscopy to study nucleoli, FUS-condensates, and poly-Q accumulations *in vivo*. Key findings include that the nucleoplasm has lower compressibility compared to the cytoplasm, despite its lower dry mass density, and that poly-Q aggregates were less compressible than FUS condensates [25].
Here, we used a combination of Brillouin microscopy and quantitative phase imaging (QPI) to investigate the impact of solution conditions, temperature, time, and amino acid sequence alterations on protein condensates in vitro, in a non-invasive, purely optical manner. We quantified changes in the molecular interaction strength in terms of Brillouin

frequency shift, and dissipative properties in terms of Brillouin linewidth. Additionally, we compute dry mass density and protein volume fraction from refractive index measurements. We found that FUS protein condensates exhibited higher values in the aforementioned optomechanical quantities in conditions with a stronger tendency for phase separation (i.e., low temperatures [26, 27], high, or low salt concentrations [28]) revealing stronger molecular interactions. We also characterized the aging process of FUS condensates and found that their dry mass density and protein volume fraction, as well as their dissipative properties, remained unaffected. The maturation process was also characterized by a gradual increase in Brillouin shift, however, this effect was much weaker than the Brillouin shift elevation due to chemical fixation. Accordingly, the observed aging process may be characterized by a progressive establishment of a crosslinked polymer network across the condensates. Finally, we showed that the molecular grammar governing macromolecular condensation also has a strong impact on the physical properties of the condensates. Our experiments with variants of the hnRNPA1 protein [29] revealed distinct values of Brillouin shift, linewidth, and dry mass density. Brillouin shifts showed a negative correlation with saturation concentrations.
Overall, we demonstrated an all-optical and label-free approach to quantify molecular interaction strength as well as dry mass density of protein condensates. We could show the sensitivity of our measurement techniques to known parameters affecting phase separation and physical properties of protein condensates. Such quantitative approaches are crucial to address open questions in the field of biological phase separation and to consolidate the current state of knowledge.

2 Results

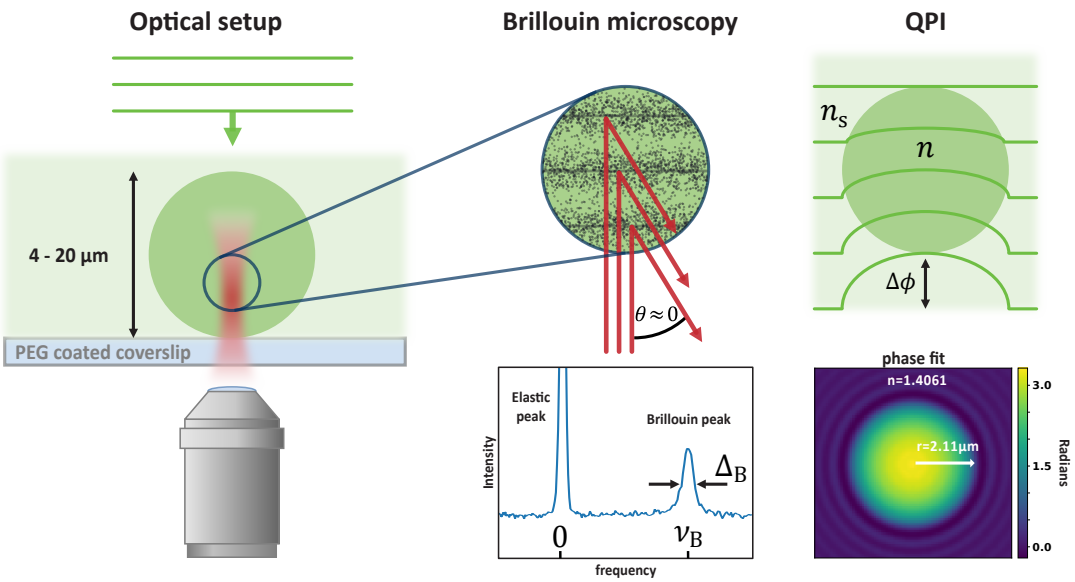

Figure 2: Introduction of experimental techniques. Left column: Schematic representation of the optical setup. Brillouin microscopy probes a single confocal spot, QPI illuminates the complete field of view with a plane wave. Middle column: Schematic representation of the Brillouin scattering process in the confocal volume probed, where θ denotes the scattering angle. The incoming probe beam is scattered by microscopic pressure waves. Brillouin frequency shift ν_B (i.e., the distance between the elastic peak and the Brillouin peak on the frequency axis) and linewidth Δ_B are indicated in an example spectrum of water. Right column: QPI quantifies the phase delay $\Delta\phi$ introduced by a specimen compared to the surrounding medium with a known refractive index n_s. A custom algorithm fits the phase image obtained, assuming a spherical shape of the specimen, providing the radius r and refractive index n of the fitted sphere (see Section 4.3 for more details).

2.1 Experimental setup

Figure 2 illustrates the experimental setup as well as the analysis workflow. Brillouin microscopy was performed by doing point measurements in the condensed and dilute phases of phase-separated protein solutions. Surface wetting of the protein was minimized by polyethylene glycol coating, keeping the condensates in a spherical shape. This enabled the use of QPI to measure the refractive index and calculate dry mass density and protein volume fraction. Furthermore, the refractive index was utilized to calculate absolute density and longitudinal modulus (see Sections 4.4 and 4.5).

2.2 Increasing temperature weakens molecular interaction strength in a polymer rich-phase

Temperature is an important thermodynamic control parameter for the formation of protein condensates. Previous reports have revealed that FUS condensation follows an upper critical solution temperature (UCST) phase diagram [27]. Therefore, we asked how temperature increase, which diminishes the driving force for phase separation [26, 27], affects the physical properties of FUS condensates.

To obtain a reference system illustrating the impact of temperature and solute concentration on the physical properties of a polymer solution, we first measured the Brillouin shift and linewidth of polyethylene glycol 3350 (PEG) solutions. We found that increasing the temperature of water (0 % PEG) or a 10 % PEG solution increased Brillouin shifts while decreasing linewidths (Figure 3A). Above a PEG concentration of 20 %, the slope Δ_B vs. ν_B became positive, yielding both an increased Brillouin shift and linewidth with lower temperatures. Our results are in line with previous Brillouin scattering measurements of PEG 600 [30] and concentrated sucrose solutions [31].

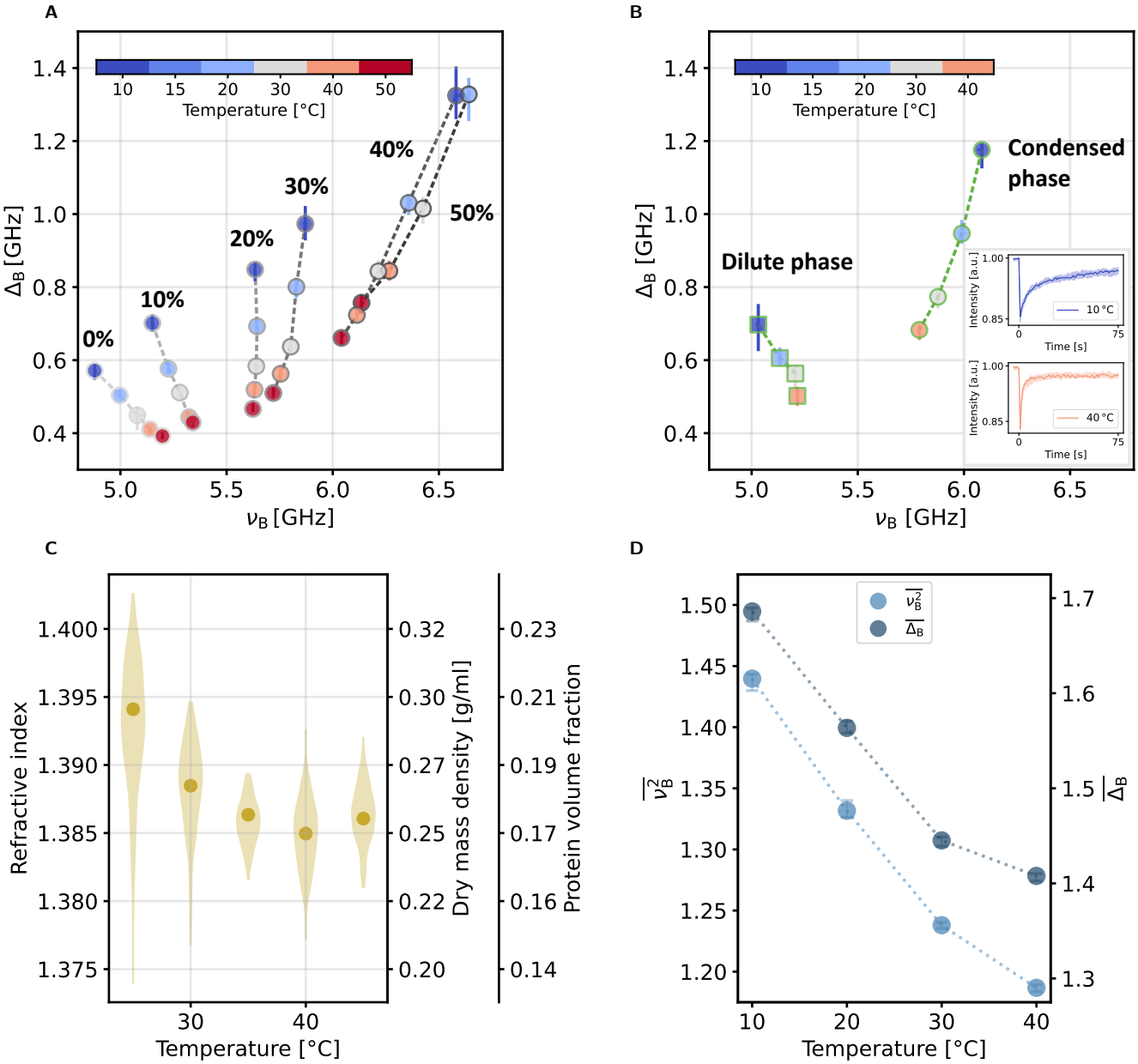

Figure 3: Temperature alterations of PEG solutions and FUS condensates. A: Brillouin linewidth and Brillouin shift for PEG solutions at different temperatures. The labels indicate the PEG weight fraction. B: Brillouin linewidth and Brillouin shift for several FUS condensates (circles) and corresponding dilute phase (squares) for different temperatures at 150 mM KCl and 5 % dextran. Inset shows fluorescence intensity recovery after photobleaching (FRAP) of FUS condensates at 10 °C and 40 °C. The solid line shows the median intensity recovery of five individual condensates. C: Corresponding refractive index, dry mass density, and protein volume fraction distributions of FUS condensates from 25 °C to 45 °C. D: Brillouin shift squared (left axis) and Brillouin linewidth (right axis) normalized to the respective values of the dilute phase. Markers indicate median values; error bars represent the range containing 68.3 % of the data points that are closest to the median. In some cases, the marker diameter is larger than the error bars.

The increase of the Brillouin shift in a dilute polymer solution due to an elevation of temperature from 10 °C to 50 °C can be explained by the viscoelastic properties of water. Water exhibits a minimum in compressibility (resulting in a maximum of the bulk modulus K) at 45 °C [32] and a vanishing shear modulus $G = 0$. Due to the relation $M = K + \frac{4}{3}G$, this implies a maximum of the longitudinal modulus [33] and accordingly in the Brillouin shift. In summary, the viscoelastic properties of water dominate at low solute concentrations up to 10 % PEG, while the solute dominates at concentrations above 20 %.

After the establishment of the PEG-model system, we conducted *in vitro* experiments on FUS condensates in the presence

of 5 % dextran to maintain the two-phase system across a broad range of temperatures. In the dilute phase of the FUS protein system (Figure 3B) we found an increase of the Brillouin shift and a reduction of the linewidth as a result of a temperature increase. The same trend was observed before for water and a 10 % PEG solution (Figure 3A). The FUS condensates on the other hand (Figure 3B), exhibited a reduction of Brillouin shift upon the same temperature change, similar to a 30 % PEG solution (Figure 3A).
Figure 3 also illustrates that the impact of polymer concentration on linewidth and Brillouin shift decreases for higher temperatures. This effect was observed for the phase-separated FUS system as well as the PEG model system. To compare our results with a widely used technique in the field, we performed fluorescence recovery after photobleaching (FRAP) to qualitatively inspect protein diffusion in the condensates. We found a faster intensity recovery at higher temperatures (Figure 3B). This observation together with the measured trends in the Brillouin linewidth shows a reduction of dissipation upon temperature increase.
In addition, we investigated whether an increase in temperature would also result in a decrease in refractive index [34] and density [35, 36] as previously reported for PEG solutions. Such behavior would be expected for a narrowing two-phase regime at increasing temperature in a UCST system. Indeed, we observed a subtle decrease in refractive index and dry mass density upon a temperature increase from 25 °C to 35 °C (Figure 3C), similar to what was reported for mEGFP-TAF15 condensates [37].
To facilitate the comparison of the different factors that were investigated in this study (temperature, ion concentration, and aging), we utilized the dilute phase for the normalization of Brillouin shift squared $\overline{\nu_B^2}$ and linewidth $\overline{\Delta_B}$ of the dense phase. Similar normalized quantities employing water as a reference were earlier introduced as "Brillouin elastic contrast" for the Brillouin shift and as "Brillouin viscous contrast" for Brillouin linewidth, respectively [38]. As the approximation $\frac{\rho}{n^2} \approx const.$ is justified in our case (see Section S 1.4 for further details), it follows that $M \approx M(\nu_B) \propto \nu_B^2$ and a measurement of the Brillouin shift is sufficient to detect changes in the longitudinal modulus. Accordingly, we report $\overline{\nu_B^2}$ instead of M as a measure of molecular interaction strength in the following text.
Plotting these normalized quantities for the phase separated FUS system as a function of temperature shows a clear reduction of $\overline{\nu_B^2}$ and $\overline{\Delta_B}$ upon temperature increase (Figure 3D). In summary, we found a reduction of molecular interaction strength and dissipative processes in condensates upon temperature increase, accompanied by a dry mass density reduction for temperatures between 25 °C and 35 °C.

2.3 Variation of ion concentration reveals three different interaction regimes

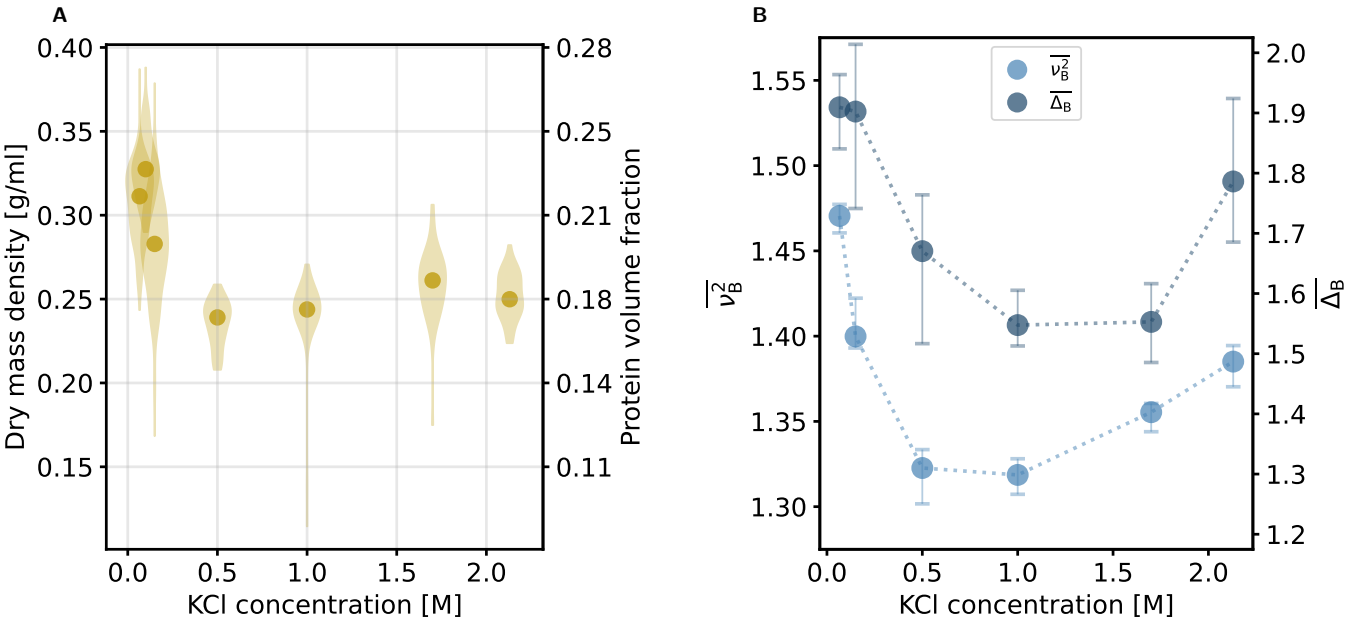

Figure 4: Impact of different KCl concentrations on FUS condensates. A: Impact of changing ionic strength on dry mass density and protein volume fraction of FUS condensates at 5 % dextran. B: Corresponding Brillouin shift squared (left axis) and Brillouin linewidth (right axis) normalized to the respective values of the dilute phase. Markers indicate median values; error bars represent the range containing 68.3 % of the data points that are closest to the median.

Another important parameter that can tune the interactions between proteins is the ion concentration in the surrounding medium. Ions have specific effects on protein-protein interactions as they directly affect the various possible interaction mechanisms of amino acids [2] and the solubilities of proteins. A previous study demonstrated that FUS exhibits a reentrant phase behavior, resulting in two phase separating regimes, one at low and another one at high ion concentrations [28]. We hypothesized that these ion-dependent interaction regimes should be also reflected in the physical properties of the FUS

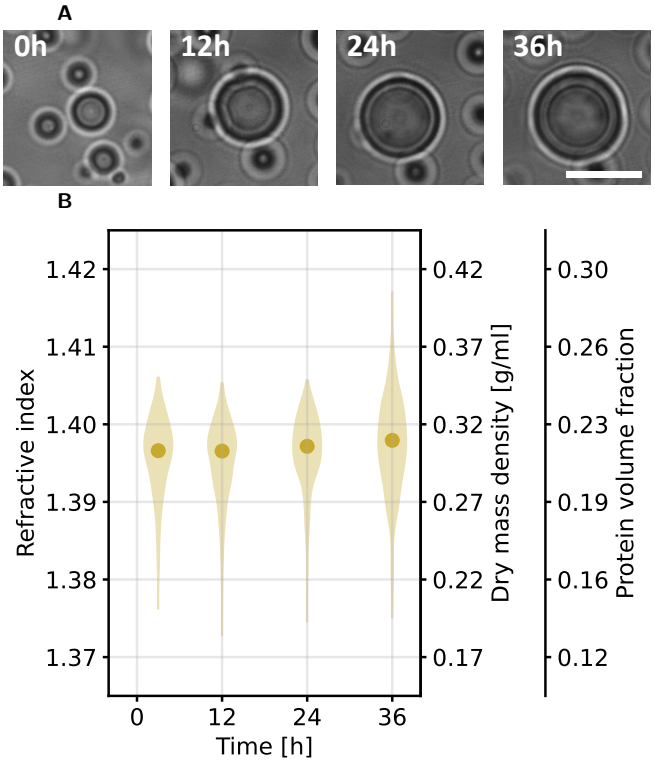

Figure 5: Effect of FUS condensate maturation on morphology and density. A: Bright-field images of a representative FUS condensate over a time course of 36 h at 150 mM KCl and 5 % dextran. B: Refractive index, dry mass density and volume fraction of FUS condensates measured 3 h, 12 h, 24 h and 36 h after condensate formation. Markers indicate median values. Scale bar: 10 µm.

condensates. As above for exploring the effect of altering temperature, we added 5 % dextran ensuring the presence of protein condensates of suitable size across the full range of KCl concentrations.

Figure 4 illustrates the distinct impact of ion concentration on the physical properties of the condensates. While the buffer solution showed a linear dependence of refractive index on ion concentration (see supplement S 1.2 and S 3A), as well as the Brillouin shift of the dilute phase (Figure S 3B), the dense phase exhibited a more complex dependence. The calculation of protein dry mass density and protein volume fraction (Figure 4A), which is based on the refractive index difference of buffer and sample (see Section 4.4), showed that the maximum of dry mass density and protein volume fraction are located at the lowest ion concentrations. Towards higher ion concentrations, in the region where FUS condensates would dissolve without the addition of a crowding agent (i.e., 0.5 M and 1 M KCl), protein dry mass density and volume fraction showed a minimum, before slightly increasing again at even higher KCl concentrations. Finally, as for the different temperatures in Figure 3, we computed normalized values for Brillouin shift squared $\overline{\nu_B^2}$ and linewidth $\overline{\Delta_B}$ (Figure 4B). Again, we identified a minimum in both quantities around a KCl concentration of 1 M, while the largest values were located at the lowest ion concentrations, similar to the trends of dry mass density and protein volume fraction.

In summary, our results show that the physical properties of the condensates change depending on interaction regime. In addition, we found that low ion concentrations lead to denser condensates with stronger molecular interactions compared to high ion concentrations.

2.4 FUS condensate aging is ion concentration dependent

Multiple publications have investigated the time dependence of viscoelastic properties of FUS protein condensates. In general, the maturation process of FUS condensates resulted in reduced protein mobility. The states of matter described for aged FUS condensates range from viscous fluids [39], and mixed liquid-gel states [40], to fibrillar solids [5, 40]. Given this broad range of results, we used Brillouin microscopy and QPI in various buffer conditions to provide an unbiased view of the aging of FUS condensates.

Previous publications reported morphological and mechanical changes in a time frame of about 12 h to 24 h [5, 39]. Accordingly, we conducted QPI measurements shortly after sample preparation, as well as 12 h, 24 h, and 36 h later. In contrast to some previous publications, we could not find morphological changes even after 36 h, other than Ostwald ripening. Accordingly, bigger condensates were growing while smaller ones were shrinking (Figure 5A). In contrast to a previous study on PGL3 condensates reporting an increase in dry mass density over time [37], we could not detect a change in refractive index, dry mass density, or protein volume fraction (Figure 5B).

We also conducted Brillouin microscopy measurements over the same time course as the QPI measurements. We were aiming to investigate the same condensate population over the whole time course. In the case that a particular condensate

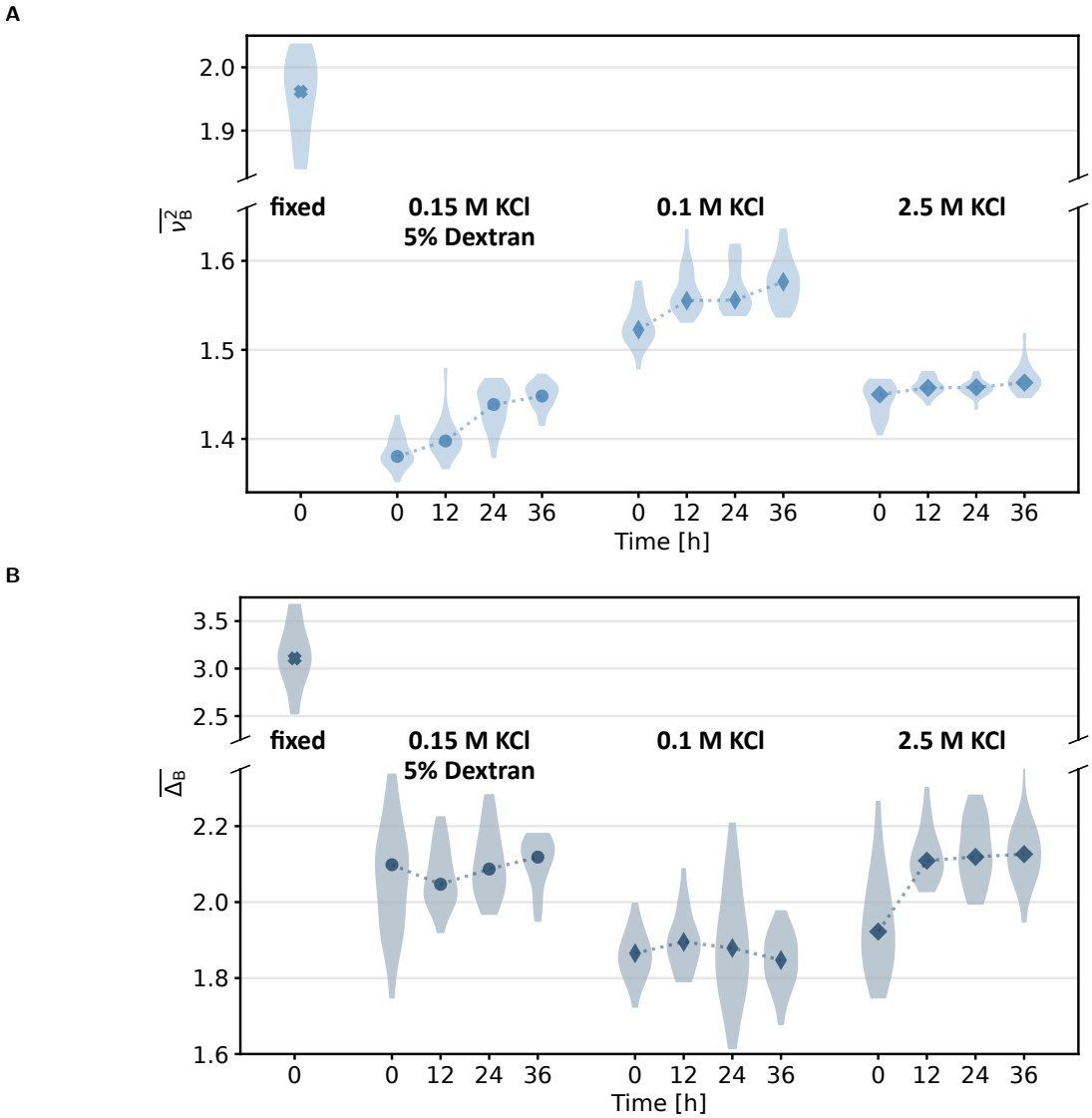

Figure 6: Effect different buffers on FUS droplet maturation. Time evolution of $\overline{\nu_B^2}$ (A) and $\overline{\Delta_B}$ (B) of FUS condensates for three different buffer conditions. Fixed condensates were chemically crosslinked by the addition of 0.05 % glutaraldehyde at a KCl concentration of 100 mM. Markers indicate median values.

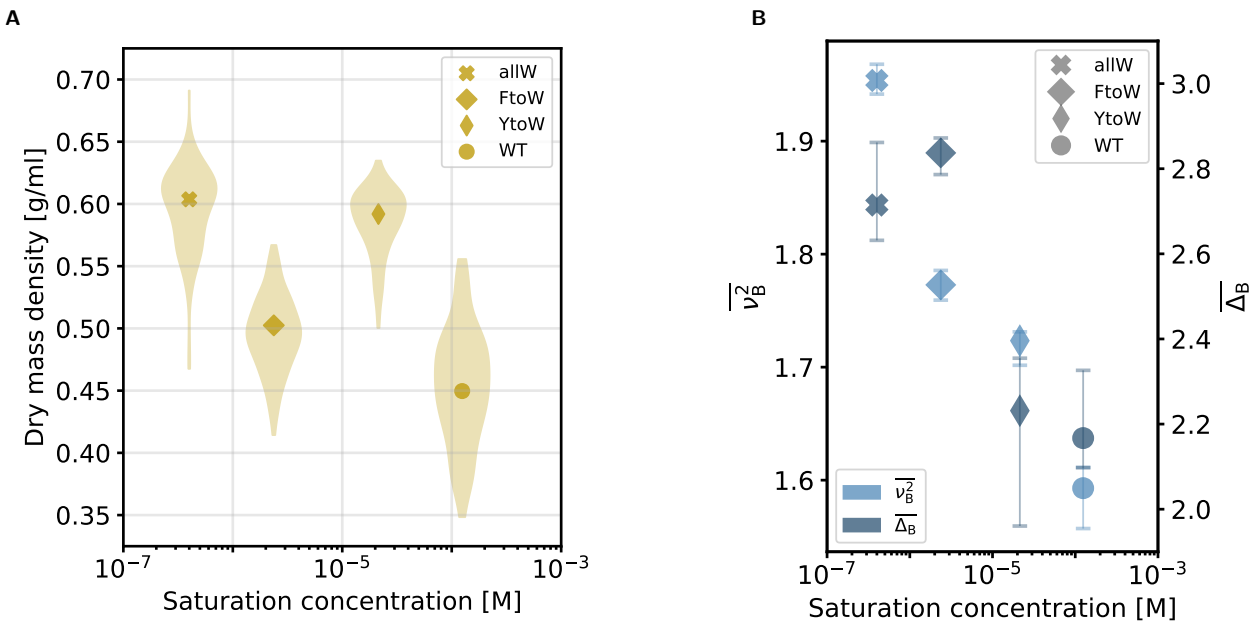

Figure 7: Physical properties of different hnRNPA1-variants against their saturation concentration. Measurements were conducted at 23 °C and 150 mM NaCl. A: Dry mass density. Refractive index and volume fraction are shown in Figure S 7. B: Brillouin shift squared (left axis) and Brillouin linewidth (right axis) normalized to the value of the dilute phase (same value for all conditions). Markers indicate median values; error bars represent the range containing 68.3 % of the data points that are closest to the median.

became inaccessible we chose a new one that was then monitored over the remaining time. To minimize any possible effects of the laser light, we chose a laser power of about 11 mW, even though much higher laser powers ($>$ 40 mW at 660 nm) have already been shown to be safe for imaging live cells [41]. As data acquisition was easier for condensates with a diameter of at least 5 µm, due to reflections caused by the refractive index jump at the condensate surface, our measurements were performed mainly on condensates that were growing (Figure 5A).

We found that the aging process of the condensates was characterized by a shallow increase in $\overline{\nu_B^2}$ of the condensate population in the case of low ion concentrations. At a KCl concentration of 2.5 M, however, this trend was suppressed (Figure 6A). Similar to the density of the condensates, the dissipative properties of the condensates were also mostly unaffected by the condensate maturation (Figure 6B). An increase in viscosity that was reported previously [39] should have been reflected in an increase in Brillouin linewidth.

To create a reference system for a completely solidified protein condensate we added 0.05 % glutaraldehyde to a phase separated FUS-protein system. To verify the solidification of the condensates we increased the temperature up to 40 °C after the measurement. As the condensates did not dissolve, we concluded that the solidification was irreversible. The chemical cross-linking led to an increase in $\overline{\nu_B^2}$ of 29 % leading to the highest value of all conditions investigated in this study.

These findings suggest that the observed ion-dependent condensate aging process is not characterized by the formation of ordered crystalline structures, or an increase in viscosity, but rather by the development of an elastic network across the condensates.

2.5 Relationship between driving force for phase separation and the optomechanical properties of condensates

To interrogate the link between the driving force for phase separation and optomechanical properties, we conducted QPI and Brillouin microscopy experiments with designed variants of the low-complexity domain of hnRNPA1 (A1-LCD). The amino acid sequences can be found in the supplement (Table S 12). The variants differ in their composition of aromatic residues, which were previously identified as main the drivers of pairwise interactions that generate three-dimensional networks and mediate homotypic phase separation in this system [42]. By substituting the other aromatic residues with tryptophan, which has the largest aromatic ring system, we were able to increase the driving force for phase separation of the resulting protein variant. In the first mutant, only the 7 tyrosine residues of the wild-type (WT) were substituted with tryptophan residues (YtoW). In a second mutant, all 12 phenylalanine residues were substituted with tryptophan residues (FtoW), further increasing the phase separation propensity. Finally, all 12 phenylalanine and 7 tyrosine residues were mutated to tryptophan residues (allW) yielding a strongly phase-separating variant. Together, these four variants provided a broad range of phase separation propensities which is reflected in a range of saturation concentrations spanning two orders of magnitude [3]. We observed an overall negative trend of the saturation concentration with the dry mass density, but no consistent correlation (Figure 7A). Figure 7B shows that $\overline{\nu_B^2}$ follows a logarithmic relationship with the

saturation concentration according to $\overline{\nu_{\mathrm{B}}^2} \approx a \log c_{\mathrm{sat}} + c$. The Brillouin linewidth, on the other hand, shows similar values for allW and FtoW, as well as for YtoW and WT, but does not follow a consistent trend with the saturation concentration. In summary, we find that altering pairwise protein-protein interaction strengths by changing the molecular grammar of protein sequences does not only change the saturation concentration but also the physical properties of the respective condensates. However, the presented data highlights that even though measured quantities are related to intermolecular interactions, they are not necessarily connected by simple relationships.

3 Discussion

In this work, we present Brillouin microscopy as a promising tool for the characterization of the physical properties of biomolecular condensates, as it introduces new ways to quantify the average interaction strength between condensate constituents. The combination with QPI offers the possibility to obtain the condensate density and allows the correct calculation of the longitudinal modulus. In contrast to other commonly employed techniques, our experimental approach is non-invasive, label-free, and can be applied *in vitro* and *in vivo*.

We showed that parameters with an impact on the phase diagram (i.e., temperature, ion concentration, and amino acid sequence) also affect the physical properties of protein condensates. Molecular interactions are therefore not only related to the saturation concentration but can be also accessed directly via the optomechanical properties of the dense phase.

In general, the absolute values of longitudinal modulus and dry mass density are relatively high for condensed biological materials. We found dry mass densities between 0.26 g/ml for FUS condensates at 0.5 M KCl and 0.60 g/ml for A1-LCD allW and longitudinal moduli between 2.65 GPa for FUS condensates at 40 °C and 4.12 GPa for A1-LCD allW. Typical dry mass densities for HeLa cells for example cover a range from about 0.07 g/ml in the nucleoplasm to 0.15 g/ml in nucleoli [43], corresponding to a longitudinal modulus of about 2.4 GPa to 2.5 GPa. Intracellular FUS condensates *in vivo* fall in the same range [25].

Similar values for dry mass density (0.26 g/ml) and longitudinal modulus (3.1 GPa) were previously found for intracellular polyQ aggregates in vivo [25]. Concentration measurements of phase-separated FUS-EGFP [44], as well as low-complexity domain molecules of FUS [45, 46] and hnRNPA1 [29, 42] found values of a few hundred mg/ml. Furthermore, a recent study employing QPI measured 0.34 g/ml for FUS-mEGFP [37] which is in line with our findings.

The differences between monocomponent condensates *in vitro* and complex multicomponent condensates in cells may underlie the substantial differences in longitudinal modulus and dry mass density observed *in vitro* compared to condensates in cells. Our study highlights the fact that the physical properties of protein condensates may be variable and context dependent, responding to external parameters such as thermodynamic variables. We also demonstrate how the physical properties can be tuned by altering the amino acid sequence. Therefore, the complex biochemical environment *in vivo* will modulate their properties, for example, due to the incorporation of additional molecules into the condensates or by post-translational modifications [47].

Uncertainties for the calculation of the density, dry mass density, and related quantities (i.e., protein volume fraction, longitudinal modulus) arise from the application of dextran as a crowding agent in some of the conditions studied (see Section S 1.6 for further details). It was found that in the absence of specific interactions and with high molecular weight crowders, depletion effects dominate and the crowder molecules are excluded from the condensates [48]. In light of these findings, the underlying assumption for our calculation of the density was that the crowder (dextran T500) is largely excluded from the protein condensates, and the values for α and θ were chosen accordingly. Nevertheless, we found that the addition of 5 % dextran resulted in a measurable reduction of refractive index, Brillouin shift, and linewidth of the FUS condensates (see Section S 1.7 for further details). Whether this difference arises from a partitioning of crowder molecules into the condensates still needs to be investigated. Furthermore, we assumed identical ion concentrations in the dilute and the dense phase. Deviations from this assumption would lead to an offset in the refractive index computation of the condensates. The impact of ion concentration on refractive index is relatively small, though (see Section S 1.2 for further details).

Our investigation of PEG solutions and phase separated FUS at different temperatures revealed characteristic behavior for different solute concentrations. We found that water dominates the response in the dilute phase of the phase separated FUS sample and in PEG solutions up to a concentration of about 10 %. For PEG concentrations higher than 20 %, and in FUS condensates, the polymers have a greater impact on viscoelasticity. This fits with the fact that both polymers have now exceeded their overlap concentrations and have entered the semi-dilute regime, greatly increasing the likelihood of interactions and entanglements [49]. Consequently, we find a decrease in Brillouin shift and linewidth upon an increase in temperature. Such behavior is also known from glass-forming liquids [50, 51]. Consistent with the decrease in Brillouin linewidth, polymer solutions typically show lower viscosities at higher temperatures [36, 52]. A reduction in viscosity with increasing temperature was also recently observed in A1-LCD condensates [3]. Here we found a reduction of the dry mass density upon a temperature increase from 25 °C to 35 °C, in line with experimental phase diagrams and findings from coarse-grained simulations of FUS condensates [53]. These results highlight that temperature strongly impacts the physical properties of the condensed phase.

We also investigated the effect of varying KCl concentrations on the physical properties of FUS condensates, as ion concentrations are a strong determinant of phase separation. In the case of FUS, the complex interplay of ion concentration

and molecular interactions leads to reentrant phase separation [28]. At a low salt concentration below 125 mM, electrostatic interactions contribute to phase separation. These interactions are shielded by the presence of higher ion concentrations. At very high KCl concentrations above 1.5 M, however, hydrophobic and non-ionic interactions drive the system again into a phase-separating regime.

Our results are in agree with these interaction regimes and further reveal the ion dependence of molecular interactions in FUS condensates. In the presence of a crowding agent, we found a drop of dry mass density in the dense phase at KCl concentrations above 100 mM associated with a drop of Brillouin shift and linewidth. Furthermore, we discovered that molecular interactions were strengthened at KCl concentrations above 1 M but did not reach the levels of the low salt conditions, even above the previously reported reentrant point of 1.5 M KCl. Also, dry mass density and volume fraction reached their maximum at the lowest ion concentrations. We conclude that the overall molecular interactions are weaker in the high salt regime. Apparently, the reduction of electrostatic interactions is not completely compensated by the hydrophobic and non-ionic interactions.

Protein condensates are metastable fluids that can undergo changes in their morphologies and material properties. This may manifest in a slowing of molecular dynamics upon condensate aging or even in the formation of solid aggregates [54]. Although the transition of the majority of FUS condensates into fibrous aggregates was previously reported to take place after 12 h [5], we only observed Ostwald ripening even 36 h after phase separation. Our observations are in agreement with the cryo-EM images of Jawerth et al. [39], where morphological changes were only occasionally visible on the condensate surface but not in the bulk material. Along the same line, recent publications suggest that the aging of FUS protein condensates is an inhomogeneous process resulting in different material properties within the same condensate [55], and solidification can be promoted by the condensate interface [40].

We found that the aging process of the FUS condensates is accompanied by an increase of the Brillouin shift at low ion concentrations, while a change in linewidth and protein volume fraction was not detected. Our results may be interpreted as increasing polymer crosslinking, similar to what was found in gelatin [51] and gelatin methacryloyl (GelMA) [56]. The change of Brillouin shift and longitudinal modulus induced by crosslinking of a polymer solution is typically small if the polymer volume fraction is kept constant [51, 57, 58]. An increase in shear viscosity as reported previously [39] should have been reflected in a larger Brillouin linewidth, although the relationship between shear viscosity and Brillouin linewidth is not straightforward [59].

Interestingly, the increase of the Brillouin shift was suppressed at a KCl concentration of 2.5 M, suggesting that a high abundance of ions attenuates the molecular interactions driving the aging process. A similar effect (i.e., suppression of aging) of high salt concentrations was previously reported for PGL-3 condensates [39]. These results suggest that the electrostatic interactions operating at low ion concentrations not only result in higher dry mass density and stronger average molecular interactions but are also important for the aging process of FUS condensates.

The chemical crosslinking via the addition of Glutaraldehyde led to a strong increase of the Brillouin shift and linewidth illustrating the effect size due to condensate solidification with covalent crosslinking. This trend would be typical for a system where the relaxation time moves into the experimentally probed timescale (i.e., sub-nanosecond in our case), and is typically caused by a loss of bulk water in biological systems. An example of such a concentration-dependent transition from a relaxed to an unrelaxed regime was found in collagen gels, where the transition onset was located at a polymer concentration of about 40 % [51].

These results suggest that the ion-dependent aging that we observed was not the transition into semi-crystalline fibers, as this would have been associated with morphological changes, a large increase in Brillouin shift, and probably changes in Brillouin linewidth and protein volume fraction.

Our investigations of A1-LCD variants with increasingly strong driving forces for phase separation revealed an overall negative trend of saturation concentration with dry mass density and Brillouin linewidth of condensates, but not an absolute correlation. Specifically, YtoW condensates have a higher density than FtoW condensates despite having a higher saturation concentration and, the FtoW variant has a higher Brillouin linewidth than may be expected compared to the YtoW and allW variants. These two observations may be related to the length scales of the underlying interactions or the modulation of hydrodynamic effects by the different types of aromatic interactions. We have recently observed a similar decoupling of viscosities from the driving force for phase separation in variants that are dominated by different types of aromatic residues [3].

The negative trend with the saturation concentration is more apparent for the Brillouin shift; hence, the interaction strength between the proteins impacts both the saturation concentration and the average molecular interaction strength within the condensed phase. A comparison of hnRNPA1 and FUS shows that the FUS protein forms less dense condensates with weaker interactions compared to the hnRNPA1 variants, although the saturation concentration of FUS is relatively low (about 2 µM at 150 mM KCl) compared to most of the A1-LCD variants. One should note here that in the case of FUS, we studied the full-length protein with a GFP-tag, not the low complexity domain in isolation.

These findings also further substantiate the sensitivity of the employed optical techniques to molecular interactions underlying phase separation. The sequence-dependent effects for dry mass density and Brillouin linewidth indicate an interesting decoupling of thermodynamics and hydrodynamics in variants that are dominated by different types of aromatic residues [3].

3.1 Outlook

The presented experimental approach has great potential to advance our understanding of the physical properties of biomolecular condensates. A powerful addition to the current instrumentation would be the possibility to detect shear waves as demonstrated by Kim et al. [60]. Then it would become feasible to directly measure the shear modulus, extract the bulk modulus from the longitudinal modulus, and derive an even more detailed physical description of the sample. Moreover, the detection of shear waves could be another modality to identify a solidification, because liquids do not allow the propagation of shear waves. The bulk quantities we measure, such as dry mass density, volume fraction, as well as sound velocity, and longitudinal modulus, may prove to be useful in refining coarse-grained simulations of condensates [29, 61, 62, 63].
Altogether, we are convinced that robust, non-invasive, and quantitative methods such as the ones presented here are crucial for the consolidation and further development of the field of biomolecular condensates. The investigation of molecular interactions and viscoelastic properties of biomolecular condensates, in particular, will pave the ground for understanding the fundamental physical principles that underlie their formation, function, and pathological relevance.

4 Materials and Methods

4.1 Protein purification

4.1.1 FUS-GFP

FUS-GFP protein was expressed from insect cells using a baculovirus expression system [64]. Cells were lysed using an LM10 Microfluidizer (Microfluidics, USA) at 10 000 psi in lysis buffer containing 50 mM Tris-HCl pH 7.4, 1 M NaCl, 5 % glycerol, 1 mM DTT, 33 U/ml of benzonase, and complete, EDTA-free Protease Inhibitor Cocktail (Merck). Lysed cells were centrifuged at 60 000 RCF for 1 h to separate soluble from insoluble fractions. The soluble fraction was bound to amylose resin (NEB, USA) for 1 h and washed with 14 column volumes of wash buffer containing 50 mM Tris-HCl pH 7.4, 1 M NaCl, 5 % glycerol, 1 mM DTT. The protein was cleaved from the MBP by loading one column volume of the same buffer supplemented with 6 µg/ml 3C protease (produced in house), and incubating for 3 h. Protein was eluted in two column volumes of the same wash buffer, and the elution fraction was concentrated to 5 ml using an Amicon Ultra Centrifugal Filter Unit (30 kDa MWCO, Merck). The concentrated protein was applied to size exclusion chromatography using a HiLoad 16/600 Superdex 200 pg (Cytiva) column on the Akta Pure (Cytiva) FPLC system in 50 mM Tris-HCl pH 7.4, 750 mM KCl, 5 % glycerol, 250 mM urea, and 1 mM DTT storage buffer. The protein was concentrated to 60 µM – 100 µM using an Amicon Ultra Centrifugal Filter Unit (30 kDa MWCO, Merck) and stored at −80 °C.

4.1.2 hnRNPA1

A1-LCD construct design and purification were carried out as described previously [3, 29]. In brief, the A1-LCD sequence was cloned into pDEST17, with a TEV cleavage site to allow for His-tag removal. Proteins were expressed in BL21(DE3) cells overnight at 37 °C using autoinduction media. The protein was purified from the insoluble fraction using denaturing buffers and nickel-chelating resin. The tag was cleaved with His-tagged TEV protease, which was removed with a second nickel column. The proteins were further purified on a size exclusion column under denaturing conditions.

4.2 Brillouin microscopy

The Brillouin microscope was already described in detail elsewhere [65]. Briefly, a diode laser (TA pro 780, Toptica, Germany) was stabilized to the D2 transition of Rubidium 85 at 780.24 nm. In order to suppress amplified-spontaneous emission, the light was transmitted through a Fabry–Pérot interferometer in two-pass configuration and guided on a Bragg-grating. The light was coupled to a Zeiss Axiovert 200 M microscope stand (Carl Zeiss, Germany) and directed to the sample trough a 40x/0.95 air objective (Carl Zeiss, Germany). The backscattered light was collected in a confocal manner and analysed with a two stage VIPA-spectrometer. We performed ca. 40-50 point measurements for several protein condensates for each condition. The number of evaluated condensates for each figure is given in the supplement (Table S 1.1). Dilute phase measurements consist of ca. 30 spectra from one location.
Data analysis was conducted with a custom software written in Python [66]. Brillouin spectra where fitted with two individual Lorentzian peaks in case of dilute phase and the sum of four Lorentzian peaks in case of protein condensates. The latter approach was necessary as in most cases also the Brillouin peaks of the dilute phase were contributing to the spectrum while all peaks were overlapping. In order to improve the quality of the fit, a measurement of the dilute phase was used to constrain the Lorentzian peaks correspondingly. Note that reported linewidths were broadened by the spectrometer and also by the distribution of scattering angles collected by the objective [67]. Temperature was controlled via a custom-built temperature stage [68].

4.3 Quantitative Phase Imaging (QPI)

Quantitative phase imaging was performed on a previously described setup [25], where only the part for optical diffraction tomography of the setup was used. It is based on Mach-Zehnder interferometry, employing a frequency-doubled Nd-YAG laser with a wavelength of 532 nm (Torus, Laser Quantum, UK). For sample illumination a 40x/1.0 water-dipping objective lens (Carl Zeiss, Germany) was used. The light diffracted by the sample was collected with a 63x/1.2 water immersion objective (Carl Zeiss, Germany). For all temperatures above room temperature (23 °C), the sample temperature was set by two foil objective heaters (Thorlabs, USA), one for each objective, controlled by a TC200 temperature controller (Thorlabs, USA).
Phase images were computed from raw holograms that were acquired at a straight angle using `qpimage` [69]. From the phase image covering the full field of view, individual FUS condensates were segmented by a custom Python software [70]. The refractive index of the individual FUS-condensates was calculated from the segmented phase images by fitting a sphere using the Rytov approximation employing `qpsphere` [71, 72]. Only droplets with a diameter greater than 2 µm were considered for the evaluation.

4.4 Density and protein volume fraction computation

The density ρ was calculated with the following formula based on a binary mixture model,

$$\rho = \frac{n - n_\mathsf{s}}{\alpha} + \rho_\mathsf{s}\left(1 - \theta\frac{n - n_\mathsf{s}}{\alpha}\right), \tag{1}$$

employing the assumption of volume additivity and the Biot mixing rule of refractive indices [65, 73]. In Equation 1, n_s denotes the refractive index of the solvent, ρ_s the density of the solvent, θ the proteins partial specific volume and α its refractive index increment. The term $[(n - n_\mathsf{s})/\alpha]$ can be identified as the dry mass density c [74, 75].
Using the information of the amino acid sequences of each protein, the values for θ and α were estimated based on the method proposed in [76] (see Table S 11). Here, instead of employing the Wiener mixing rule for dilute solutions under use in [76], the Biot mixing rule was used to maintain consistency with above Equation 1 [73]. The refractive index of the solvent was measured with an Abbe-refractometer (2WAJ, Arcarda, Germany) (see Table S 9 and Figure S 1).
The protein volume fraction (dry mass fraction) ϕ was calculated based on the dry mass density with the following formula: $\phi = \frac{V_\mathsf{dry}}{V} = \frac{m_\mathsf{dry}\theta}{V} = c\theta$.
Effects of temperature on α, θ, and ρ_s where neglected and the respective values at room temperature where used to calculate refractive index, dry mass, volume fraction and longitudinal modulus.

4.5 Longitudinal modulus computation

All measurements were performed in the back-scattering configuration, where the scattering angle θ (as defined in Figure 2) is approximately zero. Accordingly, the longitudinal modulus can be calculated by

$$M = \rho\left(\frac{\lambda\nu_\mathsf{B}}{2n\cos\theta/2}\right)^2 = \rho\left(\frac{\lambda\nu_\mathsf{B}}{2n}\right)^2 \tag{2}$$

where λ denotes the incident wavelength of 780.24 nm. Equation 2 may be also written as

$$M = ab\nu_\mathsf{B}^2 \tag{3}$$

where $a = \left(\frac{\lambda}{2\cos\theta/2}\right)^2$ denotes a setup-specific constant and $b = \frac{\rho}{n^2}$. We found variations of b in the range of only about 2 % (see Section S 1.4 for more details). Therefore, $b \approx$ const. and $M \propto \nu_\mathsf{B}^2$ are reasonable approximations in context of the presented data. For specimens with a more complex composition, where not only one type of protein is present, this approximation needs a more cautious treatment [73].

4.6 Data normalization

The values for the dilute phase, that were used to normalize longitudinal Modulus, Brillouin shift and linewidth where either obtained by the respective median value of the dilute phase (Figure 3) or by taking the value corresponding value of a linear fit (Figure 4) in order to not transfer noise from the buffer measurement to the normalized values.

4.7 Fluorescence Recovery After Photobleaching (FRAP)

FRAP experiments were carried out with an Andor spinning disc microscope (Nikon TiE inverted stand, Nikon Apo 100x, NA 1.49 Oil objective, Andor iXon+ camera) equipped with a FRAPPA unit (Andor, Northern Ireland). Temperature was controlled the same way as for the Brillouin microscopy experiments. Condensates were bleached with a 488 nm pulse with 20 µs dwell time. Fluorescence recovery was recorded in a single focal plane. For each recorded temperature recovery curves of 5 individual condensates were recorded and analyzed with a custom python software using `trackpy` to correct for stage drifting [77].

4.8 Sample preparation

4.8.1 FUS protein samples

If not stated differently, the protein stock solution (see Section 4.1.1 for further details) was diluted in a buffer containing 1 mM DTT, 20 mM PIPES at a pH of 7.4 to achieve a concentration of 5 µM FUS. If indicated, a concentration of 5 %(w/w) dextran T500 (Pharmacosmos A/S, Denmark) was used to ensure phase separation at intermediate salt concentrations and high temperatures. For imaging the sample was loaded into a chamber, built up by a PEG-coated cover slide at the bottom and a silicone spacer (Grace Bio-Labs, USA) with a height of 0.9 mm and a diameter of 4.5 mm, resulting in a sample volume of about 14 µl. PEG coating was performed according to a protocol published earlier [78]. For Brillouin microscopy and FRAP experiments, the glass surface of the temperature control stage served as the upper boundary of the sample chamber. For the QPI measurements, an untreated cover slide was used instead, as the temperature control stage was not compatible with the QPI-setup.
Condensate fixation was performed by the addition of 0.05 % Glutaraldehyde after the initialization of phase separation by dilution of the stock protein solution with water.

4.8.2 hnRNPA1 protein samples

Amicon Ultra centrifugal filters (Merck, Germany) were filled with 440 µl of 1 M MES pH 5.5 buffer. 60 µl of approximately 500 µM protein in 4 M GdmHCl was added. Filters were centrifuged for 15 min at 12 000 rcf. Afterwards, the sample was filled up to the initial volume of 500 µl with MES buffer. The centrifugation step was repeated until a 1000-fold dilution of the initial GdmHCl buffer was achieved. After the last centrifugation step, the centrifugal filter was refilled with 20 mM HEPES pH 7.0, and the previous procedure was repeated until a 10,000-fold dilution of the MES buffer was achieved. Phase separation was induced by adding NaCl to a final concentration of 150 mM. Samples were loaded on a PEG-coated cover slide and enclosed by an imaging spacer (Grace Bio-Labs, USA).

4.8.3 PEG 3350 solutions

Polyethylene Glycol (Sigma, USA) was dissolved in water to obtain a stock solution with a mass fraction of 50 %. PEG solutions with a lower mass fraction were derived from the stock solution by dilution with water. Temperature control and sample mounting were conducted as for the FUS protein samples (see Section 4.8.1).

Acknowledgements

We would like thank Felix Reichel for providing a stock solution of PEG and Anna Taubenberger for helpful discussions. Financial support from the Deutsche Forschungsgemeinschaft (SPP 2191-Molecular mechanisms of functional phase separation, grant agreement number 419138906 to SA and JG) and from the NIH (R01NS121114 to T.M.) is gratefully acknowledged.

Author contributions

The project was initiated by TB and JG; RS built the Brillouin microscope; KK built the QPI setup; PM developed essential parts of the QPI analysis software and helped with the implementation; LL purified the FUS protein; WB purified hnRNPA1 variants; RG coated the cover slides with PEG; TB conducted the experiments with help of LL, WB, KK, RS, TF, ML; CM computed refraction increment and partial specific volume of the proteins; TB analyzed and visualized the data; JG, TM and SA provided critical discussions and financial support; TB wrote the initial draft. TB edited the initial draft with help from all other authors.

Conflicts of interest

RS is an employee of the company CellSense GmbH, which develops commercial Brillouin microscopes. The other authors declare no competing interests.

References

[1] Salman F. Banani et al. "Biomolecular condensates: Organizers of cellular biochemistry". In: *Nature Reviews Molecular Cell Biology* 18.5 (2017), pp. 285–298. DOI: 10.1038/nrm.2017.7.

[2] Clifford P. Brangwynne, Peter Tompa, and Rohit V. Pappu. "Polymer physics of intracellular phase transitions". In: *Nature Physics* 11.11 (2015), pp. 899–904. DOI: 10.1038/nphys3532.

[3] Ibraheem Alshareedah et al. "Sequence-encoded grammars determine material properties and physical aging of protein condensates". In: *bioRxiv* (2023). DOI: 10.1101/2023.04.06.535902.

[4] Amandine Molliex et al. "Phase Separation by Low Complexity Domains Promotes Stress Granule Assembly and Drives Pathological Fibrillization". In: *Cell* 163.1 (2015), pp. 123–133. DOI: 10.1016/j.cell.2015.09.015.

[5] Avinash Patel et al. "A Liquid-to-Solid Phase Transition of the ALS Protein FUS Accelerated by Disease Mutation". In: *Cell* 162.5 (2015), pp. 1066–1077. DOI: 10.1016/j.cell.2015.07.047.

[6] Yun R. Li et al. "Stress granules as crucibles of ALS pathogenesis". In: *Journal of Cell Biology* 201.3 (2013), pp. 361–372. DOI: 10.1083/jcb.201302044.

[7] Hong Joo Kim et al. "Mutations in prion-like domains in hnRNPA2B1 and hnRNPA1 cause multisystem proteinopathy and ALS". In: *Nature* 495.7442 (2013), pp. 467–473. DOI: 10.1038/nature11922.

[8] Anastasia C. Murthy and Nicolas L. Fawzi. "The (un)structural biology of biomolecular liquid-liquid phase separation using NMR spectroscopy". In: *Journal of Biological Chemistry* 295.8 (2020), pp. 2375–2384. DOI: 10.1074/jbc.REV119.009847.

[9] W Russ Algar et al. "FRET as a biomolecular research tool — understanding its potential while avoiding pitfalls". In: *Nature Methods* 16.9 (2019), pp. 815–829. DOI: 10.1038/s41592-019-0530-8.

[10] Ibraheem Alshareedah, Taranpreet Kaur, and Priya R. Banerjee. "Chapter Six - Methods for characterizing the material properties of biomolecular condensates". In: *Liquid-Liquid Phase Coexistence and Membraneless Organelles*. Ed. by Christine D. Keating. Vol. 646. Methods in Enzymology. Academic Press, 2021, pp. 143–183. DOI: https://doi.org/10.1016/bs.mie.2020.06.009.

[11] Nicole O. Taylor et al. "Quantifying Dynamics in Phase-Separated Condensates Using Fluorescence Recovery after Photobleaching". In: *Biophysical Journal* 117 (7 2019). DOI: 10.1016/j.bpj.2019.08.030.

[12] Alfredo Vidal Ceballos, Charles J. McDonald, and Shana Elbaum-Garfinkle. "Chapter Two - Methods and Strategies to Quantify Phase Separation of Disordered Proteins". In: *Intrinsically Disordered Proteins*. Ed. by Elizabeth Rhoades. Vol. 611. Methods in Enzymology. Academic Press, 2018, pp. 31–50. DOI: https://doi.org/10.1016/bs.mie.2018.09.037.

[13] Ibraheem Alshareedah et al. "Programmable viscoelasticity in protein-RNA condensates with disordered sticker-spacer polypeptides". In: *Nature Communications* 12.1 (2021), p. 6620. DOI: 10.1038/s41467-021-26733-7.

[14] Louise M. Jawerth et al. "Salt-Dependent Rheology and Surface Tension of Protein Condensates Using Optical Traps". In: 121 (25 2018), p. 258101. DOI: 10.1103/PhysRevLett.121.258101.

[15] Rachel S. Fisher and Shana Elbaum-Garfinkle. "Tunable multiphase dynamics of arginine and lysine liquid condensates". In: *Nature Communications* 11.1 (2020), p. 4628. DOI: 10.1038/s41467-020-18224-y.

[16] Brillouin, Léon. "Diffusion de la lumière et des rayons X par un corps transparent homogène - Influence de l'agitation thermique". In: *Ann. Phys.* 9.17 (1922), pp. 88–122. DOI: 10.1051/anphys/192209170088.

[17] LI Mandelstam. "Light scattering by inhomogeneous media". In: *Zh. Russ. Fiz-Khim. Ova* 58.381 (1926), p. 146.

[18] Robert Prevedel et al. "Brillouin microscopy: an emerging tool for mechanobiology". In: *Nature Methods* 16.10 (2019), pp. 969–977. DOI: 10.1038/s41592-019-0543-3.

[19] Maurizio Mattarelli, Massimo Vassalli, and Silvia Caponi. "Relevant Length Scales in Brillouin Imaging of Biomaterials: The Interplay between Phonons Propagation and Light Focalization". In: *ACS Photonics* (2020). DOI: 10.1021/acsphotonics.0c00801.

[20] Irina Kabakova et al. "Brillouin microscopy". In: *Nature Reviews Methods Primers* 4.1 (2024), p. 8. DOI: 10.1038/s43586-023-00286-z.

[21] Y.P. Singh and R.P. Singh. "Compatibility studies on solutions of polymer blends by viscometric and ultrasonic techniques". In: *European Polymer Journal* 19.6 (1983), pp. 535–541. DOI: 10.1016/0014-3057(83)90206-9.

[22] Vidhya Jadhav et al. "Volumetric and compressibility studies and phase equilibria of aqueous biphasic systems of alcohols using phase diagram". In: *SN Applied Sciences* 1.7 (2019), pp. 1–12. DOI: 10.1007/s42452-019-0688-9.

[23] Giuseppe Antonacci and Sietse Braakman. "Biomechanics of subcellular structures by non-invasive Brillouin microscopy". In: *Scientific Reports* 6.37217 (2016). DOI: 10.1038/srep37217.

[24] Giuseppe Antonacci et al. "Background-deflection Brillouin microscopy reveals altered biomechanics of intracellular stress granules by ALS protein FUS". In: *Communications Biology* 1.1 (2018), p. 139. DOI: 10.1038/s42003-018-0148-x.

[25] Raimund Schüßler et al. "Correlative all-optical quantification of mass density and mechanics of subcellular compartments with fluorescence specificity". In: *eLife* 11 (2022). Ed. by Rohit V Pappu and Anna Akhmanova, e68490. DOI: 10.7554/eLife.68490.

[26] Takuya Yoshizawa et al. "Nuclear Import Receptor Inhibits Phase Separation of FUS through Binding to Multiple Sites". In: *Cell* 173.3 (2018), 693–705.e22. DOI: 10.1016/j.cell.2018.03.003.

[27] Shujie Li et al. "Pressure and Temperature Phase Diagram for Liquid–Liquid Phase Separation of the RNA-Binding Protein Fused in Sarcoma". In: *The Journal of Physical Chemistry B* 125.25 (2021), pp. 6821–6829. DOI: 10.1021/acs.jpcb.1c01451.

[28] Georg Krainer et al. "Reentrant liquid condensate phase of proteins is stabilized by hydrophobic and non-ionic interactions". In: *Nature Communications* 12.1 (2021), p. 1085. DOI: 10.1038/s41467-021-21181-9.

[29] Anne Bremer et al. "Deciphering how naturally occurring sequence features impact the phase behaviours of disordered prion-like domains". In: *Nature Chemistry* 14.2 (2022), pp. 196–207. DOI: 10.1038/s41557-021-00840-w.

[30] M. Pochylski et al. "Structuring effects and hydration phenomena in poly(ethylene glycol)/water mixtures investigated by brillouin scattering". In: *Journal of Physical Chemistry B* 110.41 (2006), pp. 20533–20539. DOI: 10.1021/jp0620973.

[31] T.J.C. Hosea, S.C. Ng, and C.G. Oates. "A Brillouin scattering study of the glass transition in sucrose". In: *Food Hydrocolloids* 4.2 (1990), pp. 137–147. DOI: 10.1016/S0268-005X(09)80014-3.

[32] Frank J. Millero, Richard W. Curry, and Walter Drost-Hansen. "Isothermal compressibility of water at various temperatures". In: *Journal of Chemical & Engineering Data* 14.4 (1969), pp. 422–425. DOI: 10.1021/je60043a018.

[33] S. C. Santucci et al. "Is there any fast sound in water?" In: *Physical Review Letters* 97.22 (2006), pp. 1–4. DOI: 10.1103/PhysRevLett.97.225701.

[34] Zdeňka Kolská et al. "Refractometric study of systems water-poly(ethylene glycol) for preparation and characterization of Au nanoparticles dispersion". In: *Arabian Journal of Chemistry* 12.8 (2019), pp. 5019–5027. DOI: 10.1016/j.arabjc.2016.11.006.

[35] Pedro Gonzalez-Tello, Fernando Camacho, and Gabriel Blazquez. "Density and Viscosity of Concentrated Aqueous Solutions of Polyethylene Glycol". In: *Journal of Chemical & Engineering Data* 39.3 (1994), pp. 611–614. DOI: 10.1021/je00015a050.

[36] Sharmin Ebrahimi and Rahmat Sadeghi. "Density, Speed of Sound, and Viscosity of Some Binary and Ternary Aqueous Polymer Solutions at Different Temperatures". In: *Journal of Chemical Engineering Data* 60.11 (2015), pp. 3132–3147. DOI: 10.1021/acs.jced.5b00290.

[37] Patrick M McCall et al. "Label-free composition determination for biomolecular condensates with an arbitrarily large number of components". In: *bioRxiv* (2023), p. 2020.10.25.352823.

[38] Giuseppe Antonacci et al. "Recent progress and current opinions in Brillouin microscopy for life science applications". In: *Biophysical Reviews* 12.3 (2020), pp. 615–624. DOI: 10.1007/s12551-020-00701-9.

[39] Louise Jawerth et al. "Protein condensates as aging Maxwell fluids". In: *Science* 370.6522 (2020), pp. 1317–1323. DOI: 10.1126/science.aaw4951.

[40] Yi Shen et al. "The liquid-to-solid transition of FUS is promoted by the condensate surface". In: *Proceedings of the National Academy of Sciences* 120.33 (2023), e2301366120. DOI: 10.1073/pnas.2301366120.

[41] Miloš Nikolić and Giuliano Scarcelli. "Long-term Brillouin imaging of live cells with reduced absorption-mediated damage at 660nm wavelength". In: *Biomedical Optics Express* 10.4 (2019), p. 1567. DOI: 10.1364/BOE.10.001567.

[42] Erik W Martin et al. "Valence and patterning of aromatic residues determine the phase behavior of prion-like domains". In: *Science* 367.6478 (2020), pp. 694–699. DOI: 10.1126/science.aaw8653.

[43] Kyoohyun Kim and Jochen Guck. "The Relative Densities of Cytoplasm and Nuclear Compartments Are Robust against Strong Perturbation". In: *Biophysical Journal* 119.10 (2020), pp. 1946–1957. DOI: 10.1016/j.bpj.2020.08.044.

[44] Jonas Ahlers et al. "The key role of solvent in condensation: Mapping water in liquid-liquid phase-separated FUS". In: *Biophysical Journal* 120.7 (2021), pp. 1266–1275. DOI: 10.1016/j.bpj.2021.01.019.

[45] Kathleen A. Burke et al. "Residue-by-Residue View of In Vitro FUS Granules that Bind the C-Terminal Domain of RNA Polymerase II". In: *Molecular Cell* 60.2 (2015), pp. 231–241. DOI: 10.1016/j.molcel.2015.09.006.

[46] Anastasia C. Murthy et al. "Molecular interactions underlying liquid-liquid phase separation of the FUS low-complexity domain". In: *Nature Structural & Molecular Biology* 26.7 (2019), pp. 637–648. DOI: 10.1038/s41594-019-0250-x.

[47] Diana M. Mitrea et al. "Modulating biomolecular condensates: a novel approach to drug discovery". In: *Nature Reviews Drug Discovery* 21.11 (2022), pp. 841–862. DOI: 10.1038/s41573-022-00505-4.

[48] Gaurav Chauhan et al. "Crowder titrations enable the quantification of driving forces for macromolecular phase separation". In: *Biophysical Journal* (2023), pp. 1–17. DOI: 10.1016/j.bpj.2023.09.006.

[49] Xue Wang et al. "Polyethylene Glycol Crowder's Effect on Enzyme Aggregation, Thermal Stability, and Residual Catalytic Activity". In: *Langmuir* 37.28 (2021), pp. 8474–8485. DOI: 10.1021/acs.langmuir.1c00872.

[50] Christoph Klieber et al. "Mechanical spectra of glass-forming liquids. II. Gigahertz-frequency longitudinal and shear acoustic dynamics in glycerol and DC704 studied by time-domain Brillouin scattering". In: *Journal of Chemical Physics* 138.12 (2013). DOI: 10.1063/1.4789948.

[51] Michelle Bailey et al. "Viscoelastic properties of biopolymer hydrogels determined by Brillouin spectroscopy: A probe of tissue micromechanics". In: *Science Advances* 6.44 (2020), eabc1937. DOI: 10.1126/sciadv.abc1937.

[52] W. R. Moore. "Viscosity-Temperature Relationships for Dilute Solutions of High Polymers". In: *Nature* 191.4795 (1961), pp. 1292–1293. DOI: 10.1038/1911292b0.

[53] Han Yi Chou and Aleksei Aksimentiev. "Single-Protein Collapse Determines Phase Equilibria of a Biological Condensate". In: *Journal of Physical Chemistry Letters* 11.12 (2020), pp. 4923–4929. DOI: 10.1021/acs.jpclett.0c01222.

[54] Simon Alberti and Anthony A. Hyman. "Biomolecular condensates at the nexus of cellular stress, protein aggregation disease and ageing". In: *Nature Reviews Molecular Cell Biology* 22.3 (2021), pp. 196–213. DOI: 10.1038/s41580-020-00326-6.

[55] Adiran Garaizar et al. "Aging can transform single-component protein condensates into multiphase architectures". In: *Proceedings of the National Academy of Sciences* 119.26 (2022), e2119800119. DOI: 10.1073/pnas.2119800119.

[56] Maryam Alsadat Rad et al. "Micromechanical characterisation of 3D bioprinted neural cell models using Brillouin microspectroscopy". In: *Bioprinting* 25 (2022), e00179. DOI: 10.1016/j.bprint.2021.e00179.

[57] A. Bot, R. P. C. Schram, and G. H. Wegdam. "Brillouin light scattering from a biopolymer gel: hypersonic sound waves in gelatin". In: *Colloid & Polymer Science* 273.3 (1995), pp. 252–256. DOI: 10.1007/BF00657831.

[58] J. P. Jarry and G D Patterson. "Brillouin scattering from polyepoxide solutions and gels". In: *Macromolecules* 14.5 (1981), pp. 1281–1284. DOI: 10.1021/ma50006a026.

[59] Jennifer Illibauer et al. "Longitudinal viscosity of blood plasma for rapid COVID-19 prognostics". In: *medRxiv* (2023). DOI: 10.1101/2023.10.13.23297016.

[60] Moonseok Kim et al. "Shear Brillouin light scattering microscope". In: *Optics Express* 24.1 (2016), p. 319. DOI: 10.1364/OE.24.000319.

[61] Zakarya Benayad et al. "Simulation of FUS Protein Condensates with an Adapted Coarse-Grained Model". In: *Journal of Chemical Theory and Computation* 17.1 (2021), pp. 525–537. DOI: 10.1021/acs.jctc.0c01064.

[62] Mina Farag et al. "Condensates formed by prion-like low-complexity domains have small-world network structures and interfaces defined by expanded conformations". In: *Nature Communications* 13.1 (2022), p. 7722. DOI: 10.1038/s41467-022-35370-7.

[63] Giulio Tesei et al. "Accurate model of liquid–liquid phase behavior of intrinsically disordered proteins from optimization of single-chain properties". In: *Proceedings of the National Academy of Sciences* 118.44 (2021). DOI: 10.1073/pnas.2111696118.

[64] Régis P. Lemaitre et al. "FlexiBAC: A versatile, open-source baculovirus vector system for protein expression, secretion, and proteolytic processing". In: *BMC Biotechnology* 19.1 (2019), pp. 1–11. DOI: 10.1186/s12896-019-0512-z.

[65] Raimund Schlüßler et al. "Mechanical Mapping of Spinal Cord Growth and Repair in Living Zebrafish Larvae by Brillouin Imaging". In: *Biophysical Journal* 115.5 (2018), pp. 911–923. DOI: 10.1016/j.bpj.2018.07.027.

[66] Raimund Schlüßler and others. *BMicro*. Version 0.8.1. 2023. URL: https://github.com/BrillouinMicroscopy/BMicro.

[67] Giuseppe Antonacci et al. "Spectral broadening in Brillouin imaging". In: *Applied Physics Letters* 103.22 (2013). DOI: 10.1063/1.4836477.

[68] Matthäus Mittasch et al. "Non-invasive perturbations of intracellular flow reveal physical principles of cell organization". In: *Nature Cell Biology* 20.3 (2018), pp. 344–351. DOI: 10.1038/s41556-017-0032-9.

[69] Paul Müller. *qpimage*. Version 0.7.5. 2022. URL: https://pypi.org/project/qpimage/0.7.5/.

[70] Timon Beck. *DropletQPI*. Version 0.1.0. 2023. URL: https://github.com/GuckLab/DropletQPI.

[71] Paul Müller et al. "Accurate evaluation of size and refractive index for spherical objects in quantitative phase imaging". In: *Optics Express* 26.8 (2018), p. 10729. DOI: 10.1364/OE.26.010729.

[72] Paul Müller. *qpsphere*. Version 0.5.8. 2021. URL: https://pypi.org/project/qpsphere/0.5.8/.

[73] Conrad Möckel et al. "Estimation of the mass density of biological matter from refractive index measurements". In: *bioRxiv* (2023). DOI: 10.1101/2023.12.05.569868.

[74] R. BARER. "Interference Microscopy and Mass Determination". In: *Nature* 169.4296 (1952), pp. 366–367. DOI: 10.1038/169366b0.

[75] H. G. Davies and M. H. F. Wilkins. "Interference Microscopy and Mass Determination". In: *Nature* 169.4300 (1952), pp. 541–541. DOI: 10.1038/169541a0.

[76] Huaying Zhao, Patrick H. Brown, and Peter Schuck. "On the distribution of protein refractive index increments". In: *Biophysical Journal* 100.9 (2011), pp. 2309–2317. DOI: 10.1016/j.bpj.2011.03.004.

[77] Daniel B. Allan et al. *soft-matter/trackpy: Trackpy v0.5.0*. Version v0.5.0. 2021.

[78] Simon Alberti et al. "A User's Guide for Phase Separation Assays with Purified Proteins". In: *Journal of Molecular Biology* 430.23 (2018). Phase Separation in Biology and Disease, pp. 4806–4820. DOI: 10.1016/j.jmb.2018.06.038.

S 1 Supplement

S 1.1 Number of evaluated samples

Temperature [°C]	10	20	30	40
N	7	8	8	8

Table S 1: Number of evaluated condensates n in Figure 3B and 3D.

Temperature [°C]	25	30	35	40	45
N	344	274	239	134	205

Table S 2: Number of evaluated condensates n in Figure 3C.

KCl conc. [M]	0.066	0.1	0.15	0.5	1	1.7	2.13
N	143	84	525	57	71	43	39

Table S 3: Number of evaluated condensates n in Figure 4A.

KCl conc. [M]	0.066	0.15	0.5	1	1.7	2.13
N	10	31	12	30	31	29

Table S 4: Number of evaluated condensates n in Figure 4B.

Time point [h]	3	12	24	36
N	525	555	482	428

Table S 5: Number of evaluated condensates n in Figure 5B.

Condition	fixed	0.15 M KCl 5 % dextran				0.1 M KCl				2.5 M KCl			
Time point [h]	0	0	12	24	36	0	12	24	36	0	12	24	36
N	11	31	29	36	35	30	31	28	29	32	30	31	32

Table S 6: Number of evaluated condensates n in Figure 6A and 6B.

Variant	allW	FtoW	YtoW	WT
N	133	290	396	176

Table S 7: Number of evaluated condensates n in Figure 7A.

Variant	allW	FtoW	YtoW	WT
N	9	9	10	10

Table S 8: Number of evaluated condensates n in Figure 7B.

S 1.2 Derivation of refractive index and density of buffer solutions

H_2O			H_2O + 5 % dextran		
KCl [M]	n	ρ [g/ml]	KCl [M]	n	ρ [g/ml]
0	1.334	0.997	0	1.334	1.0218
0.5	1.339	1.01977	0.5	1.346	1.0405
1	1.344	1.04134	1	1.351	1.0593
1.5	1.3485	1.06189	1.7	1.3585	1.078
2	1.3535	1.08152	2.13	1.362	1.0969
2.5	1.3585	1.10031			
3	1.362	1.11832			
3.5	1.3665	1.13562			

Table S 9: Refractive index and density of aqueous KCl solutions. Refractive index values (second and fifth column) where measured with an Abbe-refractometer at room temperature. Density values in the third column were taken from literature [1] and were measured at 25 °C. Density values in the sixth column were calculated via Equation 1, with $\alpha_{\text{dextran}} = 0.14\,\text{ml/g}$ [2] and $\theta_{\text{dextran}} = 0.5959\,\text{ml/g}$ [3].

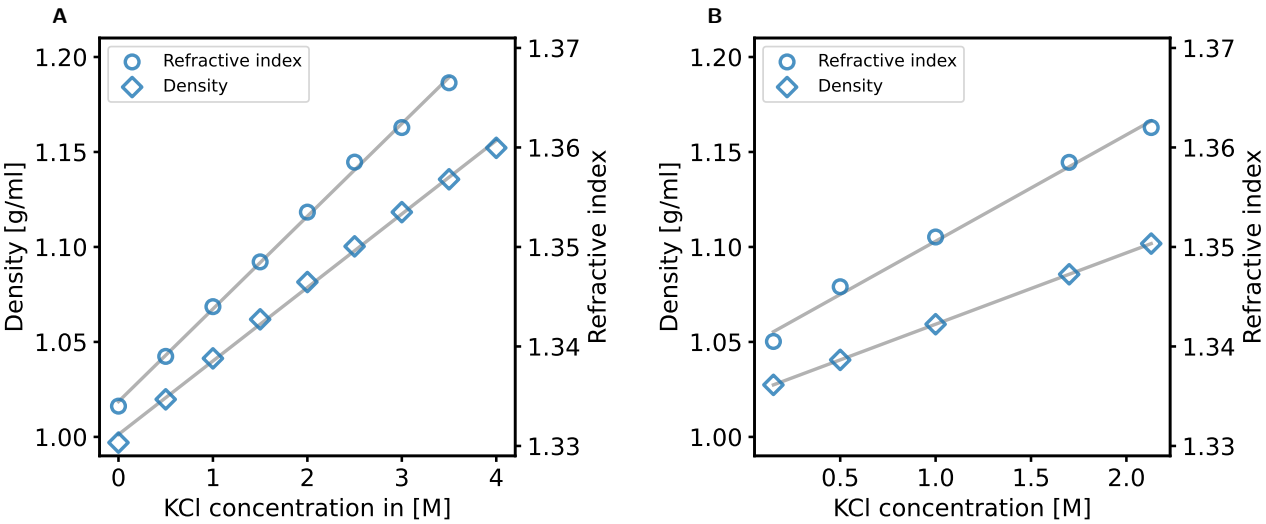

Figure S 1: Density and refractive index of aqueous KCl solutions. Values were taken from Table S 9. Refractive index and density for KCl dissolved in water (A) and KCl dissolved in water with the addition 5 % dextran (B). Fitting parameters for the linear fits are displayed in Table S 10.

coefficient	n	ρ	n_{Dex}	ρ_{Dex}
a	0.0093 M^{-1}	0.0387 g/(ml M)	0.0107 M^{-1}	0.0376 g/(ml M)
b	1.3345	1.0013 g/ml	1.3399	1.0218 g/ml

Table S 10: Linear fitting parameters for refractive index and density. Parameters were calculated according to the equation $y = ax + b$, were y denotes either refractive index or density and x denotes the KCl concentration.

S 1.3 Refractive index increment and partial specific volume of the studied proteins

Protein	FUS-GFP	allW	FtoW	YtoW	WT
α [ml/g]	0.199469	0.215825	0.21149	0.207454	0.203518
θ [ml/g]	0.704177	0.67979	0.676467	0.682987	0.681031

Table S 11: Refractive index increment α and partial specific volume θ for FUS-GFP and the investigated hnRNPA1 variants. Calculations were carried out as described in [4] based on the amino acid sequence.

S 1.4 Longitudinal modulus scaling

As already mentioned in the methods section 4.4 we used formula 1 to compute the mass density $\rho = \rho(n, \alpha, \theta)$, which establishes a linear relationship with the refractive index n. Keeping the refraction increment α and the partial specific volume θ constant it follows the commonly used approximation $\frac{\rho}{n^2} \approx const.$ for small changes of n. Note that this assumption is only valid for dilute protein solutions. Other substances as for example lipids exhibit different values for α and θ. Consequently, the assumption $\nu_B^2 \propto M$ is not valid for samples possessing heterogeneous α and θ distributions, as for example adipocytes [5]. Figure S 2A illustrates the relative change of $\frac{\rho}{n^2}$ for the most extreme values of n appearing in this study using equation 1. We found changes of $\frac{\rho}{n^2}$ in the range of 2 %. Due to this small change of $\frac{\rho}{n^2}$ we found a linear correlation of ν_B^2 and M (Figure S 2B). Values for n_s, ρ_s which were required for the calculation of the mass density based on Equation 1, were interpolated from the second and third column of Table S 9, respectively.

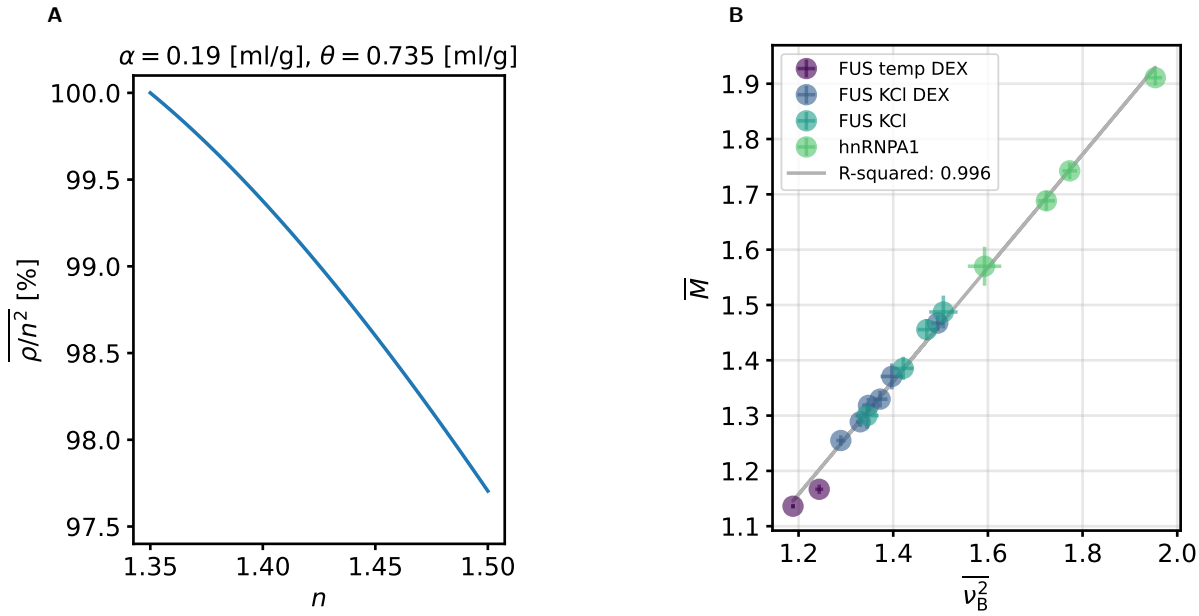

Figure S 2: Impact of density and refractive index on longitudinal modulus computation. A: Relative changes of $\frac{\rho}{n^2}$ over the range of observed refractive index values. B: Correlation of normalized longitudinal Modulus with the normalized Brillouin shift squared. The presented values correspond to Figure 3D (FUS temp DEX), Figure 4B (FUS KCl DEX), Figure S 5B (FUS KCl) and Figure 7B (hnRNPA1), respectively. Error bars are based on Equation S 1 and the standard deviation of ν_B.

The longitudinal modulus calculation was based on Brillouin shift, refractive index, refractive index increment and partial specific volume, e.g., $M = M(\nu_B, n, \alpha, \theta)$. The only contributions of random uncertainties originated from the measurements of Brillouin shift and refractive index. Based on the Gaussian error propagation we used the following formula to quantify the random uncertainties of the longitudinal modulus:

$$\Delta M = \sqrt{\left(\frac{\partial M}{\partial \nu_B}\Delta\nu_B\right)^2 + \left(\frac{\partial M}{\partial n}\Delta n\right)^2} \tag{S 1}$$

S 1.5 Supplementary figures for FUS condensates at different KCl concentrations

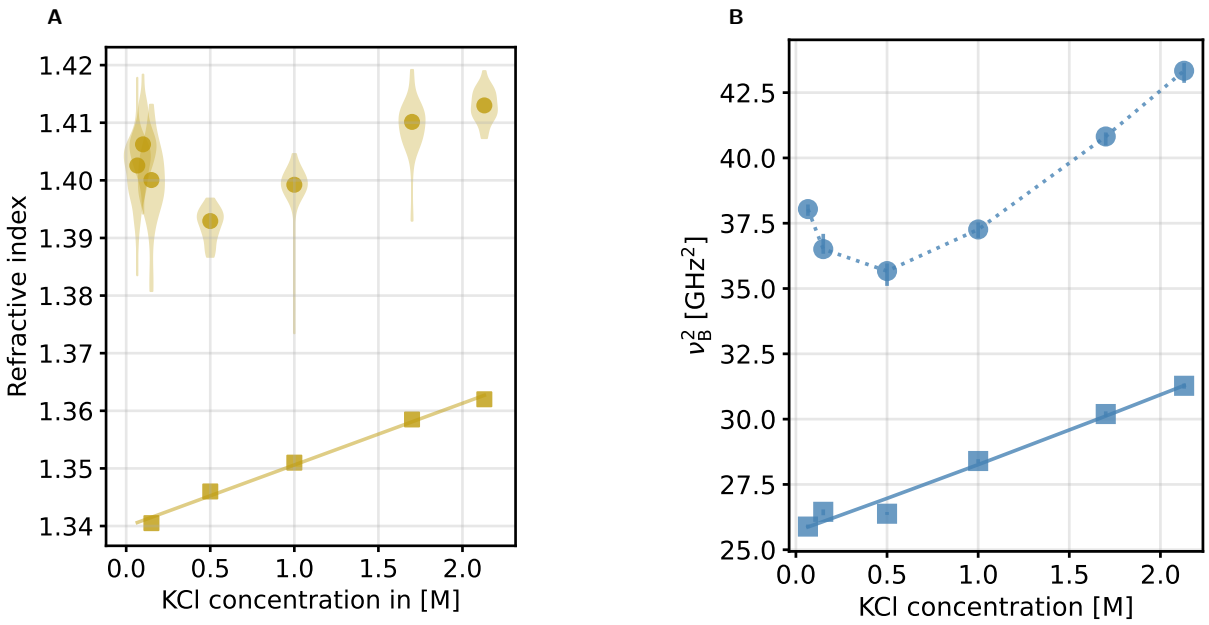

Figure S 3: Comparison of buffer and FUS condensates. A: Refractive index values FUS condensates (circles) and buffer (squares) for various KCl concentrations. B: Corresponding values of Brillouin shift squared showing FUS condensates (circles) and dilute phase (squares). Markers indicate median values; error bars represent the range containing 68.3 % of the data points that closest to the median.

S 1.6 Uncertainties of the density computation

As already mentioned, deviations from the calculated density values may arise from the presence of dextran in the condensate (in case dextran was added to the buffer). The presence of dextran in the condensates would alter the effective values of refraction increment α and partial specific volume θ (i.e., $\alpha_{\text{dextran}} \approx 0.14\,\text{ml/g}$ [2], $\theta_{\text{dextran}} \approx 0.6\,\text{ml/g}$ [3]; $\alpha_{\text{protein}} \approx 0.19\,\text{ml/g}$, $\theta_{\text{protein}} \approx 0.735\,\text{ml/g}$ [6]). The effect of these uncertainties on the calculation of the (dry) mass density is illustrated in Figure S 4.

Furthermore, ion concentration was assumed to be equal in dilute and dense phase. As the presence of ions has an impact on the refractive index, a non-uniform distribution of ions across the two phases would lead to an offset in the refractive index computation of the condensates. However, as this impact is relatively small (for KCl in water we found $\mathrm{d}n\,/\,\mathrm{d}c = 0.0093\,\mathrm{M}^{-1}$, see Table S 10), we believe that this effect is likely negligible. Finally, the quantities α and θ might exhibit a certain variability upon changing ion and temperature conditions [7, 8, 9] that was not taken into account.

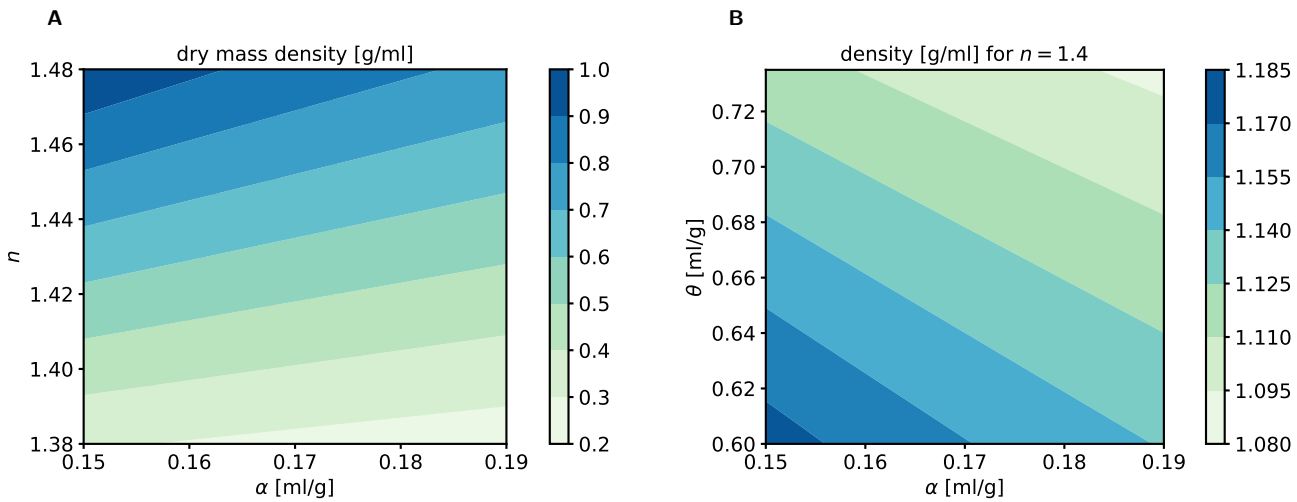

Figure S 4: Impact of refractive index increment and partial specific volume on density computation. A: Dry mass density for different values of refractive index and refraction increment. B: Absolute density for mixtures of dextran and FUS for a given refractive index. Lower left of the plot corresponds to pure dextran, the upper right to pure FUS.

S 1.7 Reference measurements of FUS condensates without dextran

In order to check the effect of dextran on the physical properties of FUS condensates we compared suitable conditions with and without the presence of dextran. While trends were qualitatively maintained, we found an offset due to the addition of dextran. In fact, we found that Brillouin shift and linewidth (Figure S 5), as well as refractive index (Figure S 6), dry mass density, and protein volume fraction of the FUS condensates were affected by the presence of a 5 % dextran concentration. As phase separation was suppressed for temperatures above 30 °C and for intermediate ion concentrations, we could not acquire data in those regimes.

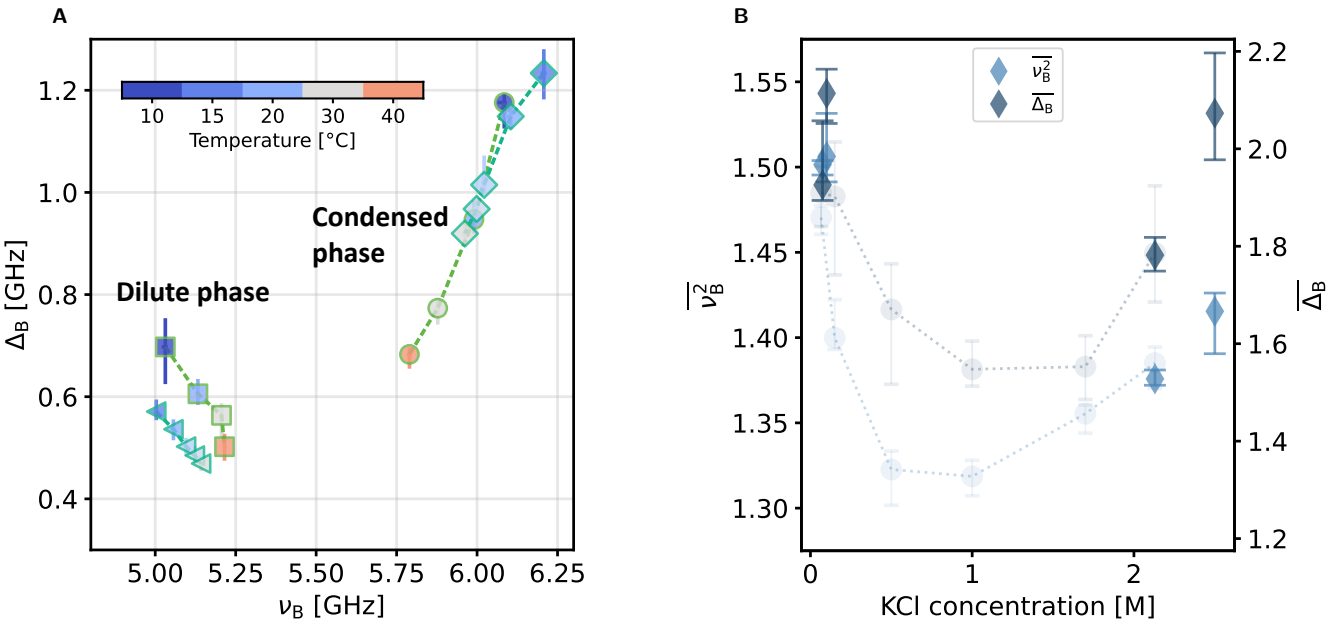

Figure S 5: Evaluation of the impact of 5 % dextran on Brillouin microscopy results. Values for Brillouin shift and linewidth of dilute and condensed phase for various temperatures (A) and KCl concentrations (B). Triangles correspond to Dilute phase, diamonds show the condensed phase. Squares and circles correspond to the respective values with 5 % dextran in the buffer as presented in the main text. Temperature in (B) was 20 °C, KCl concentration in (A) was 150 mM. Markers indicate median values; error bars represent the range containing 68.3 % of the data points that closest to the median.

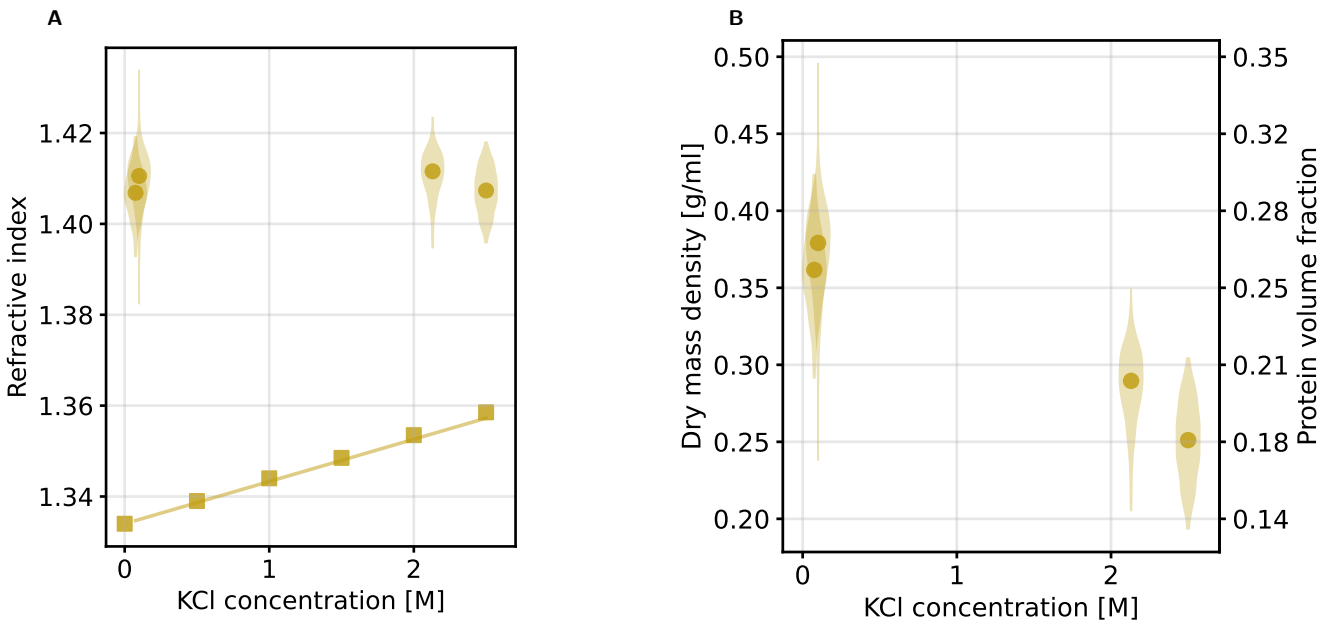

Figure S 6: QPI measurements of FUS condensates. A: Refractive index of buffer and FUS protein condensates at different KCl concentrations. B: Corresponding dry mass density and protein volume fraction. Circles represent median values of FUS condensates, squares single measurements with a refractometer of the buffer solution.

S 1.8 Amino Acid sequences of hnRNPA1 variants

variant	sequence
WT	GSMASASSSQRGRSGSGNFGGGRGGGFGGNDNFGRGGNFSGRGGFGGSRGGGGY GGSGDGYNGFGNDGSNFGGGGSYNDFGNYNNQSSNFGPMKGGNFGGRSSGPYGG GGQYFAKPRNQGGYGGSSSSSSYGSGRRF
FtoW	GSMASASSSQRGRSGSGNWGGGRGGGWGGNDNWGRGGNWSGRGGWGGSRGGGGY GGSGDGYNGWGNDGSNWGGGGSYNDWGNYNNQSSNWGPMKGGNWGGRSSGGSGG GGQYWAKPRNQGGYGGSSSSSSYGSGRRW
YtoW	GSMASASSSQRGRSGSGNFGGGRGGGFGGNDNFGRGGNFSGRGGFGGSRGGGGW GGSGDGWNGFGNDGSNFGGGGSWNDFGNWNNQSSNFGPMKGGNFGGRSSGGSGG GGQWFAKPRNQGGWGGSSSSSSWGSGRRF
allW	GSMASASSSQRGRSGSGNWGGGRGGGWGGNDNWGRGGNWSGRGGWGGSRGGGGW GGSGDGWNGWGNDGSNWGGGGSWNDWGNWNNQSSNWGPMKGGNWGGRSSGGSGG GGQWWAKPRNQGGWGGSSSSSSWGSGRRW

Table S 12: Amino acid sequences of the studied low complexity domains of hnRNPA1.

S 1.9 Refractive index and protein volume fraction of hnRNPA1 condensates

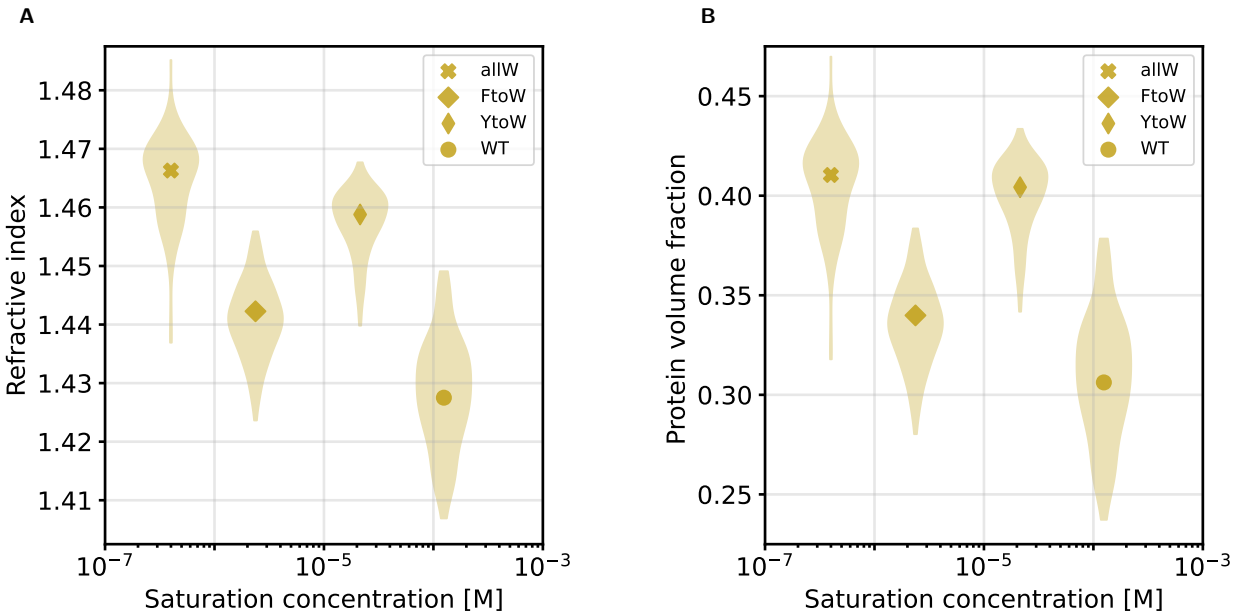

Figure S 7: QPI measurements of hnRNPA1 condensates. Refractive index (A) and protein volume fraction (B) of hNRNPA1 condensates at 23 °C and 150 mM NaCl. Markers indicate median values.

References

[1] Lisa A. Romankiw and I Ming Chou. "Densities of aqueous sodium chloride, potassium chloride, magnesium chloride, and calcium chloride binary solutions in the concentration range 0.5-6.1 m at 25, 30, 35, 40, and 45 °C". In: *Journal of Chemical & Engineering Data* 28.3 (1983), pp. 300–305. DOI: 10.1021/je00033a005.

[2] Arno Max Basedow, Klaus Heinrich Ebert, and Ursula Ruland. "Specific refractive index increments of dextran fractions of different molecular weights". In: *Die Makromolekulare Chemie* 179.5 (1978), pp. 1351–1353. DOI: 10.1002/macp.1978.021790523.

[3] Frank Doebert, Andreas Pfennig, and Matthias Stumpf. "Derivation of the Consistent Osmotic Virial Equation and Its Application to Aqueous Poly(ethylene glycol)-Dextran Two-Phase Systems". In: *Macromolecules* 28.23 (1995), pp. 7860–7868. DOI: 10.1021/ma00127a037.

[4] Conrad Möckel et al. "Estimation of the mass density of biological matter from refractive index measurements". In: *bioRxiv* (2023). DOI: 10.1101/2023.12.05.569868.

[5] Raimund Schüßler et al. "Correlative all-optical quantification of mass density and mechanics of subcellular compartments with fluorescence specificity". In: *eLife* 11 (2022). Ed. by Rohit V Pappu and Anna Akhmanova, e68490. DOI: 10.7554/eLife.68490.

[6] Huaying Zhao, Patrick H. Brown, and Peter Schuck. "On the distribution of protein refractive index increments". In: *Biophysical Journal* 100.9 (2011), pp. 2309–2317. DOI: 10.1016/j.bpj.2011.03.004.

[7] Gertrude E. Perlmann and L. G. Longsworth. "The Specific Refractive Increment of Some Purified Proteins". In: *Journal of the American Chemical Society* 70.8 (1948), pp. 2719–2724. DOI: 10.1021/ja01188a027.

[8] Tsutomu Arakawa. "Calculation of the Partial Specific Volumes of Proteins in Concentrated Salt, Sugar, and Amino Acid Solutions". In: *The Journal of Biochemistry* 100.6 (1986), pp. 1471–1475. DOI: 10.1093/oxfordjournals.jbchem.a121853.

[9] Ingrid Pilz and Gertrud Czerwenka. "The partial specific volume of various proteins and its dependence on concentration and temperature of the solution". In: *Die Makromolekulare Chemie* 170.1 (1973), pp. 185–190. DOI: 10.1002/macp.1973.021700115.